Continental hyperextension, mantle exhumation and thin oceanic crust at the continent-ocean transition, West Iberia: new insights from wide-angle seismic.

R. G. Davy[1], T. A. Minshull[1], G. Bayrakci[1], J. M. Bull[1], D. Klaeschen[2], C. Papenberg[2], T. J. Reston[3], D. S. Sawyer[4], C. A. Zelt[4].

1. University of Southampton, Southampton, United Kingdom.

2. GEOMAR Helmholtz Centre for Ocean Research, Kiel, Germany.

3. University of Birmingham, Birmingham, United Kingdom.

4. RICE University, Houston, TX, United States of America.

Key Points:

1) West of the Peridotite Ridge, exhumed mantle is present over a short distance (< 25 km), landward of the onset of an anomalously thin oceanic crust (0.5 – 1.5 km thick), which thickens seaward.
2) We assign an upper bound to the age of the thin oceanic crust of 122 Ma, based on the dating of materials recovered from the Peridotite Ridge. This age is consistent with continental breakup progressing from south to north along the Iberian margin.
3) The S-reflector detachment surface possesses undulations that correlate with the pattern of high and low-velocity regions below this surface. This velocity structure is interpreted to be the result of preferential mantle hydration along normal faults.

Abstract

Hyperextension of continental crust at the Deep Galicia rifted margin in the North Atlantic has been accommodated by the rotation of continental fault blocks, which are underlain by the S-reflector, an interpreted detachment fault, along which exhumed and serpentinized mantle peridotite is observed. West of these features, the enigmatic Peridotite Ridge has been inferred to delimit the western extent of the continent-ocean transition. An outstanding question at this margin is where oceanic crust begins, with little existing data to constrain this boundary and a lack of clear seafloor spreading magnetic anomalies. Here we present results from a 160-km-long wide-angle seismic profile (WE-1). Travel-time tomography models of the crustal compressional velocity structure reveal highly thinned and rotated crustal blocks separated from the underlying mantle by the S-reflector. The S-reflector correlates with the 6.0 – 7.0 kms^{-1} velocity contours, corresponding to peridotite serpentinization of 60 – 30 %, respectively. West of the Peridotite Ridge, shallow and sparse Moho reflections indicate the earliest formation of an anomalously thin oceanic crustal layer, which increases in thickness from ~0.5 km at ~20 km west of the Peridotite Ridge to ~1.5 km, 35 km further west. P wave velocities increase smoothly and rapidly below top basement, to a depth of 2.8 – 3.5 km, with an average velocity gradient of 1.0 s^{-1}. Below this, velocities slowly increase toward typical mantle velocities. Such a downward increase into mantle velocities is interpreted as decreasing serpentinization of mantle rock with depth.

1. Introduction

Rifted continental margins are delimited by the continent-ocean transition (COT), a zone separating unextended continental crust and unambiguous oceanic crust. The present day morphology of the crust and mantle in these areas gives insight into the extensional processes which lead to the failure of continental crust and the onset of seafloor spreading [*Buck*, 1991]. To understand these processes, it is critical to image structural deformation within COT and

define both its inner and outer extents. Many studies of late-stage rift processes and deformation structures have been conducted at ultra-slow extending margins, where geophysical imaging is not impeded by voluminous magmatic processes [*Whitmarsh et al.*, 1996; e.g. *Dean et al.*, 2000; *Zelt et al.*, 2003; *Van Avendonk et al.*, 2006]. However, ultra-slow extension margins pose a challenge, with low magma supply resulting in wide transitional zones suggested to comprise of either exhumed and serpentinized upper mantle materials, or anomalously thin oceanic crust underlain by serpentinized mantle, which can be difficult to discriminate without physical sampling [*Van Avendonk et al.*, 2006]. Wide-angle seismic studies of zones of exhumed continental mantle have shown that seismic velocities rapidly increase to ~7.6 kms^{-1} within a few kilometers of top basement [*Minshull*, 2009]. These velocities are too high to be explained by magmatic underplating at such shallow depths, and is better explained by seawater penetrating and serpentinizing the unroofed mantle peridotite [*Christensen*, 2004]. However, velocities also increase rapidly to > 7.6 kms^{-1}, within a few kilometers of top basement, in areas of anomalously thin oceanic crust [*Mutter and Mutter*, 1993; *Funck et al.*, 2003]. These two basement types are sometimes distinguished from one another by the presence of, frequently weak, Moho reflections and seafloor spreading magnetic anomalies, which are attributed to the presence of oceanic crust [*Sibuet et al.*, 1995; *Pickup et al.*, 1996].

Where mantle exhumation is observed before the onset of normal seafloor spreading, the process responsible for the switch from mantle exhumation to seafloor spreading is currently poorly understood. However, observations and numerical modeling of magma-poor rift margins have shown that the extension rate may have an influence on the generation of magmatic melt and/or the exhumation of mantle materials [e.g. *Bown and White*, 1995; *Minshull et al.*, 2001; *Pérez-Gussinyé*, 2013]. Exhumation of mantle occurs at ultra-slow extension rates of < 10 mm/yr (< ~6.4 mm/yr in most observed data), while extension/spreading

half-rates of > 10 mm/yr promote the generation of magmatic melt, which may be sufficient to accrete oceanic crust [*Pérez-Gussinyé et al.*, 2006; *Sibuet et al.*, 2007; *Pérez-Gussinyé*, 2013].

The Iberia-Newfoundland conjugate rifted margin is considered the archetype of magma-poor rift margins; the COT at the Iberia margin is characterized by extreme thinning of the crust (continental hyperextension), detachment faulting and the exhumation of continental mantle materials over wide areas [*Whitmarsh et al.*, 2001a; *Pérez-Gussinyé*, 2013; *Peron-Pinvidic et al.*, 2013; *Minshull et al.*, 2014]. At the conjugate Newfoundland margin the COT is much narrower [e.g. *Hopper et al.*, 2004; *Shillington et al.*, 2006; *Van Avendonk et al.*, 2006; *Van Avendonk et al.*, 2009]. Zones of mantle exhumation are observed within COT on both conjugate margins, landward of unequivocal oceanic crust [e.g. *Dean et al.*, 2000; *Van Avendonk et al.*, 2006].

Geophysical studies at the Deep Galicia margin have documented comprehensively the progressive extension, deformation and thinning of the continental crust, but no survey has extended far enough oceanward to positively identify unequivocal oceanic crust, leaving the oceanward extent of the COT undetermined. *Sibuet et al.* [1995] inferred the presence of thin oceanic crust west of the Peridotite Ridge from magnetic modeling that implied the presence of high magnetizations (5 A/m). *Whitmarsh et al.* [1996] used sparsely sampled reflection and refraction data to infer the presence of an anomalously thin oceanic crust (2.5 – 3.5 km thick), underlain by a serpentinized peridotite body, directly west of the Peridotite Ridge, and oceanic crust of normal thickness (7 km) around 20 km oceanward. Recently *Dean et al.* [2015] interpreted new multichannel seismic data west of the Peridotite Ridge. Based on basement morphology, these authors identified five ridge-like structures and propose that these structures formed through a combination of processes, starting with the continued exhumation of mantle material, transitioning to episodic volcanism which produced thin oceanic crust and the exhumation of oceanic core complexes [*Dean et al.*, 2015]. Much remains to be understood

about the nature of transitional crust in these distal zones of ultra-slow extending/spreading margins, the deformation processes which bring mantle to the seafloor, and the processes which control the eventual onset of seafloor spreading.

This paper presents new wide-angle seismic data, coincident with the multichannel seismic images of *Dean et al.* [2015]. These data extend c. 90 km west of the Peridotite Ridge and reveal new insights into the nature of the basement within the COT at the Deep Galicia margin.

2. Tectonic setting

The Iberia – Newfoundland ultra-slow spreading rift system is responsible for the opening of the North Atlantic Ocean. Rifting at this margin occurred in two primary phases, the earliest occurred in the Late Triassic - Early Jurassic [*Pérez-Gussinyé et al.*, 2003; *Tucholke et al.*, 2007; *Mohn et al.*, 2015]. Magnetic anomaly modeling and stratigraphic records show that rifting progressed from south to north [*Masson and Miles*, 1984; *Whitmarsh and Miles*, 1995; *Mohn et al.*, 2015]. During the first rifting phase, several fault-bound rift basin were formed in pure-shear environments on the proximal margins of the rift system (e.g. Lusitanian, Porto and Galicia Interior basins) [*Murillas et al.*, 1990; *Péron-Pinvidic et al.*, 2007; *Tucholke et al.*, 2007]. A second major episode of rifting initiated in the Late Jurassic - Early Cretaceous. During this period of extension, thinning and deformation of the continental lithosphere shifted from a broad region to focused areas at the distal margins, where the continental crust would eventually rupture [*Tucholke et al.*, 2007; *Mohn et al.*, 2015]. Extension focused on the future Iberian distal margin and resulted in the continental crust thinning to less than 10 km. In its entirety, this thinning occurred over distances of 100 – 200 km [*Reston*, 2009]. Conversely, at the conjugate Newfoundland margin, thinning was abrupt, focused over a distance of ~50 km, and is suggested to give rise to the asymmetric rift geometry [*Hopper et al.*, 2004; *Van Avendonk et al.*, 2006; *Van Avendonk et al.*, 2009]. Some authors have suggested that this

structural asymmetry may be exaggerated by the final line of continental breakup, leaving the bulk of thinned crust on the Iberian margin [*Reston*, 2009; *Reston*, 2010].

Focused extension and embrittlement of the continental crust on the Iberian margin led to the formation of concave downward detachment faults which exhumed mantle rock to the seafloor [*Whitmarsh et al.*, 2001b; *Lavier and Manatschal*, 2006; *Péron-Pinvidic et al.*, 2007; *Reston*, 2007a]. Initial seafloor half-spreading rates are calculated to be 7 mm/yr, and it is proposed that this ultra-slow rate has resulted in either the exhumation of large areas of mantle materials, or anomalously thin oceanic crust [*Whitmarsh et al.*, 1996; *Dean et al.*, 2000; *Srivastava et al.*, 2000; *Hopper et al.*, 2004; *Shillington et al.*, 2006; *Van Avendonk et al.*, 2006; *Pérez-Gussinyé*, 2013]. Timing of the eventual continental breakup and the onset of seafloor spreading between Iberia and Newfoundland is still widely debated, and varies along the margin [*Peron-Pinvidic et al.*, 2013]. In the southern Iberia Abyssal Plain, *Dean et al.* [2000] used seismic refraction and reflection data to identify the earliest oceanic crust, corresponding to the M3 magnetic anomaly (~130 Ma). Consistent with this interpretation, *Russell and Whitmarsh* [2003] interpreted the M3 anomaly to be the first widespread sea-floor magnetic anomaly. However, IODP drilling in the southern Iberia Abyssal Plain, and the conjugate Newfoundland margin, revealed the presence of serpentinized mantle peridotite at, or seaward of the M3 magnetic anomaly [*Whitmarsh et al.*, 2001b; *Tucholke and Sibuet*, 2007]. *Sibuet et al.* [2007] attributes these linear anomalies to the ability of serpentinites to record magnetic reversals. *Minshull et al.* [2014] revisited seismic constraints in the southern Iberia Abyssal Plain and assigned an age of 125-127 Ma to the earliest oceanic crust.

Typically the onset of oceanic spreading can be identified by the first magnetic field reversal (isochron) recorded by the earliest oceanic crust. However, the late stages of continental extension and the eventual breakup of the continent, at the Iberia-Newfoundland margin, occurred during the Cretaceous constant polarity interval (121-83 Ma), resulting in a lack of

147 strong magnetic reversals which would enable the clear identification of oceanic crust [*Bronner*
148 *et al.*, 2011; *Granot et al.*, 2012]. The J anomaly is the most prominent magnetic anomaly
149 observed within the COT at both the Iberia and Newfoundland margin (Figure 1B). This
150 anomaly is interpreted as the beginning of the M sequence of seafloor spreading anomalies
151 (M0-M3), or alternatively as the result of a pulse of magmatism that led to continental breakup
152 before seafloor spreading [*Sibuet et al.*, 2007; *Bronner et al.*, 2011]. The J anomaly is well
153 defined in the southern Iberia Abyssal Plain, but rapidly decreases in amplitude north of IAM-
154 9, and is not observed at the Deep Galicia margin.

155 In the Southern Iberia Abyssal Plain (Figure 1B), south of the Deep Galicia margin, wide-angle
156 seismic data (Figure 1B) reveals a very broad continent-ocean transition, which possesses a
157 ~190 km wide zone of exhumed mantle between extended continental crust and the onset of
158 anomalously thin oceanic crust [*Dean et al.*, 2000; *Minshull et al.*, 2014]. The SCREECH
159 seismic experiment (Figure 1A) has also revealed the presence of exhumed mantle at the
160 eastern margin of the Grand Banks, the direct conjugate margin to the Southern Iberia Abyssal
161 Plain [*Van Avendonk et al.*, 2006]. The zones of exhumed continental mantle observed at the
162 Grand Banks margin are found to be varied in width; 80 km on SCREECH line 3 and ~25 km
163 on SCREECH line 2, to the north [*Shillington et al.*, 2006; *Van Avendonk et al.*, 2006]. Both
164 of these margins have been sampled by drilling; at the Newfoundland margin by ODP leg 210
165 (inset Figure 1A) [*Tucholke et al.*, 2004]; and at the Iberia margin by ODP legs 149 and 173
166 (Figure 1B and 1C) [*Sawyer et al.*, 1994; *Whitmarsh et al.*, 1998]. Sites from these drilling
167 expeditions are situated within the COT at each margin and many sites recovered serpentinized
168 mantle peridotite. Sites 1277 and 1070 were drilled on outer highs, at the oceanward limit of
169 the COT at the Newfoundland and Iberia margins, respectively, and recover exhumed mantle
170 interspersed with intrusive mafic material.

171 At the Deep Galicia margin, continued extension of the continental lithosphere was
172 accommodated by a complex pattern of faulting, resulting in extreme crustal thinning from
173 ~30 km to just a few km over distances of 100 - 200 km [*Reston*, 2009]. Initial extension is
174 inferred to have been accommodated on high angle normal faults, forming large rotated fault
175 blocks (10-20 km wide) where the crust was between 20-30 km thickness [*Ranero and Pérez-*
176 *Gussinyé*, 2010]. How continued extension was accommodated by fault structures is still
177 debated, with sequential and polyphase faulting being the two primary mechanisms proposed
178 [*Ranero and Pérez-Gussinyé*, 2010; *Reston and McDermott*, 2014]. The latter authors propose
179 that with continued extension, blocks of continental crust, bound by normal faults, were rotated
180 to low angles to a point where the faults locked up, and new preferentially oriented faults were
181 cut through the existing faults and fault blocks [*Reston*, 2007b; *Reston and McDermott*, 2014].
182 In the sequential faulting mechanism, continued extension either reactivated existing faults,
183 rotating them to lower angles, or cut new preferentially oriented faults through the thinned
184 crust, but not cutting previous faults. Deformation at any one time is focused on a single fault,
185 with successive faults cutting through crust thinned by the preceding fault, resulting in a
186 migrating rift center and the formation of hyperextended crust, giving rise to an asymmetric
187 rift system [*Ranero and Pérez-Gussinyé*, 2010; *Pérez-Gussinyé*, 2013].

188 As the crust continued to extend, thin and cool, the ductile mid- and lower-crust became
189 progressively brittle, becoming completely brittle once the continental crust was < 10 km thick,
190 commonly referred to as hyperextension, coupling the entire crust and enabling concave down
191 listric faults to penetrate through to the underlying mantle [*Pérez-Gussinyé and Reston*, 2001;
192 *Pérez-Gussinyé et al.*, 2003; *Pérez-Gussinyé*, 2013]. Such faults acted as conduits, allowing
193 the hydration of the upper mantle and formation of a layer of structurally weak serpentinized
194 mantle [*Pérez-Gussinyé and Reston*, 2001]. As a result, listric faults (responsible for hydrating
195 the mantle) soled out into this structurally weak layer, forming a large detachment fault, known

196 as the S-reflector, oriented at a low angle (< 20^0) [*Reston et al.*, 2007]. In the final stages of
197 rifting, serpentinized subcontinental mantle was exhumed to the seafloor along the S-reflector.
198 Immediately seaward of the S-reflector is the Peridotite Ridge, which is suggested to mark the
199 landward limit of oceanic crust [*Sibuet et al.*, 1995; *Whitmarsh et al.*, 1996]. The Peridotite
200 Ridge was sampled by ODP site 637 during ODP leg 103, and returned serpentinized mantle
201 peridotite [*Boillot et al.*, 1987]. At the Flemish Cap, the conjugate to the Deep Galicia margin,
202 data from the SCREECH 1 seismic profile was used to interpret a ~50 km wide transition zone
203 comprised of anomalously thin oceanic crust underlain by partially serpentinized upper mantle
204 [*Hopper et al.*, 2004]. These previous studies of the Iberia – Newfoundland margin suggest
205 that the continent-ocean transition decreases in width northwards, but the oceanward limit of
206 the transition zone has not yet been delimited at the Deep Galicia margin.

207 ## 3. Data acquisition and processing

208 ### 3.1 GALICIA-3D and ISE-1 – Wide angle and reflection datasets

209 The Galicia 3D project was a joint multichannel seismic (MCS) reflection and wide angle
210 seismic experiment performed between 1 June 2013 and 2 August 2013. 3D multichannel
211 reflection seismic data were recorded over an area of 65 x 25 km by the RV Marcus G.
212 Langseth, while an array of 72 ocean bottom seismometers and hydrophones (OBS/H), from
213 the UK Ocean Bottom Instrumentation Facility (OBIF) [*Minshull et al.*, 2005] and GEOMAR,
214 recorded wide angle seismic arrivals. This survey area, referred to here as the 3D Box,
215 encompasses geologic features of interest such as the S-reflector detachment fault, hyper-
216 extended continental crust and the Peridotite Ridge.

217 The focus of this paper is on a 2D seismic line, a subset of the Galicia 3D dataset, which runs
218 through the 3D Box and extends an additional ~90 km westward (Figure 1C); the entire length
219 of which is 157 km and is referred to as Western Extension 1 (WE-1). Thirty-two OBS/H were

deployed on the WE-1 multichannel seismic profile, which is coincident with the western limit of the ISE-1 seismic line (Figure 1C) [*Sawyer et al.*, 1997; *Zelt et al.*, 2003] . The easternmost section of WE-1 consisted of 17 instruments within the 3D Box, spaced densely at ~1.7 km intervals, with the intention to produce a high detail 2D velocity model of the seismic structure above and below the S-reflector. The central section of WE-1 comprised 9 OBS, spaced at distances of ~3.4 km, covering the Peridotite Ridge and the sedimentary basins on its western and eastern flanks. The western section of WE-1 comprised 6 OBS, spaced ~9.7 km apart. The intention of this western section was to produce seismic images and a velocity model westward of the Peridotite Ridge, in order to resolve the nature of basement and potentially identify the landward limit of oceanic crust. OBIF and GEOMAR instruments record at a frequency of 250 Hz and 200 Hz, respectively. Two of the 32 OBS were not retrieved, while another three instruments returned no usable data. The seismic source comprised two 3,300 cu. in. air gun arrays, towed at a depth of 9 m. A total of 2,727 shots were recorded along WE-1. Within the 3D box the two gun arrays were fired alternately every 37.5 m (a shot interval of ~16 s), for high resolution 3D reflection imaging. Outside the 3D Box, the source for the 2D line was a single 3,300 cu. in. gun array fired every 150.0 m (an interval of ~64 s), with the aim of yielding data with a higher signal-to-noise ratio, for the purpose of tomography modeling.

Several other datasets have been collected at the Galicia margin, most notably the Iberia Seismic Experiment (ISE) dataset, collected in 1997, which consists of wide-angle and MCS data [*Sawyer et al.*, 1997; *Zelt et al.*, 2003]. ISE-1 is a 2D profile, coincident with the eastern section of WE-1; the western limit of the shooting line terminates 10 km west of the Peridotite Ridge, and extends 335 km eastward (Figure 1B). Eight OBH from this study lie along the eastern section of WE-1, spaced 4–10 km apart (8 km on average). During the ISE-1 profile, shots from an 8,385 cu. in. gun array were fired every 60 s, approximately four times the interval of the shots within the 3D Box of Galicia-3D experiment. A larger source array and

greater shot interval in the ISE experiment produced seismic records with higher signal-to-noise ratio (Figure 2), enabling travel time picks to greater offset, and thus improving the depth of tomographic imaging within the 3D box. For these reasons, the ISE-1 data were used to complement the WE-1 dataset. The final tomography modeling utilized a total of 34 OBS/H.

3.2 Data processing

For each instrument, clock drifts were determined and corrected for using GPS synchronized clocks. OBS/H were relocated to adjust for any variation in the deployment position during the ~5 km descent through the water column. The relocation procedure minimized the least squares misfit between the observed direct water wave arrival to each instrument and those calculated for depths determined from bathymetry collected during the Galicia-3D survey. On average each instrument was relocated by 315 m. Within the 3D Box there is a low signal-to-noise ratio (Figure 2), which is a result of poorly attenuated noise in the water column from the previous shot. In order to improve the signal-to-noise ratio, a minimum phase Ormsby band-pass filter (2-4-8-16Hz) was applied to all receiver gathers.

4 Data analysis

4.1 Phase identification and picking

In order to build a compressional velocity model of WE-1, the P wave arrivals through the subsurface must be correctly identified. These arrivals were best observed on the hydrophone channel of the OBS/H and therefore this channel was used for travel time picking. Confident identification of refracted and reflected arrivals through post-rift sediments is made difficult by the depth of the sea-floor (4.2 – 5.3 km), a thin sedimentary cover along the seismic profile (< 1.0 – 2.0 km) and interference from high-amplitude earlier seismic arrivals. Where sediment refractions were identified, they have apparent velocities up to 3.0 kms^{-1}. We identified and picked 758 sediment refraction picks and 655 reflection picks from a prominent inter-

sedimentary reflector. Crustal refractions east of the Peridotite Ridge have apparent velocities > 4.5 kms^{-1}, and highly varied travel time arrivals owing to extreme basement topography (rotated fault blocks). A reduction velocity of 8 kms^{-1} was applied to help correlate the boundary between crustal and mantle arrivals, with mantle arrivals appearing horizontal in reduced data sections (Figure 3). However, beneath the S-reflector the mantle is serpentinized, which results in mantle arrivals with apparent velocities varying from ~6.0 kms^{-1} to ~8.0 kms^{-1}. West of the Peridotite Ridge all instruments, excepting 73, exhibit seismic arrivals with apparent velocities > 7.0 kms^{-1} arriving at short offsets of 13.0 km or less. Between these high-velocity arrivals and the direct arrival, limited linear refractions with apparent velocities of 4.5 kms^{-1} – 5.0 kms^{-1} are observed. We assume that the apparent velocity of 4.5 kms^{-1} is associated with the top of the reflective basement. The travel times of these high-velocity seismic arrivals show high lateral variability, which correlates strongly with the basement topography observed in the seismic reflection data. First arrival travel times observed west of the Peridotite Ridge quickly reach apparent velocities of > 7.0 kms^{-1}, with little evidence of velocities indicative of continental crust; we refer to these as basement arrivals (Pb). We identified and picked 9,517 first arrival travel times from prominent seismic refractions through the crust, basement and mantle (e.g. Pg, Pb and Pn). The velocity contrast between thin continental crust and underlying mantle at the S-reflector generates reflections that are considered to be PmP arrivals. A total of 1,187 near-vertical reflections from the S-reflector (PmP) were identified and picked after the direct arrival, without the application of a band-pass filter; band pass filtering causes the coda from the direct arrival and other arrivals to coalesce with the S-reflection coda, prohibiting accurate identification.

Picking uncertainties are assigned for each dataset, based on the inspection of individual traces and their offset from the recording OBS/H. Table 1 details the pick uncertainty, relative to offset, assigned to each dataset and the average pick uncertainty.

294 4.2 Sedimentary arrivals

295 A lack of clear refraction and reflection arrivals from the sedimentary layering resulted in a
296 tomographic inversion with little constraint in the post-rift sedimentary layers, a lack of
297 definition at the top of the basement and a sparse resolution of sedimentary velocities.
298 Therefore for the sediment cover along WE-1, we developed a forward model using the code
299 of *Zelt and Smith* [1992]. This model utilizes top basement depths from the MCS images of
300 *Dean et al.* [2015], reflected arrivals from the top of basement, a consistent inter-sedimentary
301 layer boundary, and limited refracted arrivals from the lower sedimentary layer. We assumed
302 that seismic velocities are laterally homogeneous along the profile. Model layers and their
303 associated velocities were adjusted to minimize the misfit between calculated and observed
304 travel times. The final sediment velocity model (Figure 4) has a RMS travel time misfit of
305 67 ms and a chi-squared ($\chi 2$) value of 1.38. Sediment velocities in the upper layer increase
306 from 2.0 to 2.1 kms $^{-1}$, while in the bottom layer these velocities increase from 2.3 to 2.6 kms^{-1}.

307 4.3 Basement arrivals

308 Tomographic modeling of crustal structure was performed using "TOMO2D", the joint
309 reflection and refraction inversion algorithm of *Korenaga et al.* [2000]. This method allows
310 the determination of a 2D velocity field by simultaneous inversion of both first arrival travel
311 times and later reflected arrivals from a geological interface. The iterative tomographic
312 inversion process requires an input velocity and interface model, and observed refraction and
313 reflection travel times.

314 The input velocity model is defined by a sheared mesh which hangs from the seafloor
315 bathymetry. Model cell size is 250 m in the horizontal direction, while the vertical size
316 increases from 25 m directly below the seafloor, to 250 m at the base of the model at 15 km
317 depth. We used the sediment velocity model from forward modeling to define the shallow

structure in the input model, below which velocity smoothly increases from 4.5 kms^{-1} (below the top of reflective basement) to 8.3 kms^{-1} at 12.5 km model depth, and 8.4 kms^{-1} at 15.0 km depth. The velocity of 4.5 kms^{-1} at the top of basement was chosen based on observations of refracted arrivals observed on instruments west of the Peridotite Ridge. In this model the S-reflector is treated as the Moho, and a floating reflector, representing the surface of the S-reflector, is arbitrarily defined as a horizontal line at a depth of 7 km, with node spacing of 250 m. Extensive parameter testing was undertaken in order to find the simplest, geologically reasonable model with low travel time misfit to the observed data. From these results we selected horizontal correlation lengths that increase from 2.0 km at the seafloor to 4.0 km at the base of the model, and vertical correlation lengths increasing from 0.5 km at the seafloor to 1.0 km at the base of the model. A depth weighting kernel of 0.2 was selected to favor velocity perturbations over interface depth perturbations. Sedimentary velocities were allowed to vary through the inversion process. Travel-time pick and misfit statistics for the final 2D velocity model (Figure 5) are detailed in Table 2. No individual instrument has a RMS travel time misfits exceeding 98 ms. Individual travel time misfits rarely exceed 200 ms, and exhibit a significant reduction in travel time misfit between the input and final velocity models (Figure 6).

4.4 Resolution and accuracy

Tomography modeling produces a non-unique velocity model, with uncertainty introduced from travel times picking, the input velocity model and the model parameterization. Therefore it is critical to assess the resolution and accuracy of the final velocity model.

4.4.1 Derivative weight sum

Ray coverage through the final velocity model is represented by the derivative weight sum (DWS). There is an excellent ray coverage east of the Peridotite Ridge (95 – 150 km) at depths

between 6 and 10 km (Figure 7), encompassing the S-reflector. Moderate ray coverage is observed west of the Peridotite Ridge (20 – 95 km) at depths of 6 – 10 km. Below 10 km depth the ray coverage is often moderate to poor, with many of the model cells being sampled solely by unidirectional ray paths. High derivative weight sums west of the Peridotite Ridge are observed at a depths between 12.0 - 12.5 km, and show rays travelling through a limited range of depths. These rays come solely from instrument 38 and 40, east of the Peridotite Ridge, which have RMS travel time misfits of 37 ms and 81 ms, respectively.

4.4.2 Monte Carlo uncertainty analysis

Monte Carlo uncertainty testing [*Korenaga et al.*, 2000] enables us to assess quantitatively the uncertainty associated with the final compressional velocity model. Uncertainty in the velocity model arises from a combination of error in data picking, the starting model used, and the geometry and execution of the seismic experiment [*Zhang and Toksöz*, 1998; *Sallarès et al.*, 2011]. For our compressional velocity model we performed one hundred inversion realizations, which required the generation, and tomographic inversion, of 100 randomized input velocity models, randomized reflector depths, and "noisy" travel-time datasets. Input velocity models were generated by randomizing the original input model by ± 5% the original velocities, resulting in velocities of ± 0.10 kms^{-1} at the top of the sedimentary layers, ± 0.23 kms^{-1} at the top of reflective basement, and ± 0.42 kms^{-1} at the base of the model. The depth of the input reflector, representing the S-reflector, was randomized by ± 2.0 km. "Noisy" travel-time datasets were generated by adding randomized timing errors, including a common receiver error (± half the maximum receiver error, with a maximum of ± 58 ms), and picking errors (± half the individual pick error) [*Zhang and Toksöz*, 1998; *Korenaga et al.*, 2000]. Then, the tomographic inversion was repeated for randomized velocity model, reflector depth, and noisy travel-time dataset triples, using the same inversion parameters which generated the final velocity model (Figure 5). The mean deviation of all 100 realizations can be interpreted as a

statistical measure of the uncertainty in the averaged velocity model (Figure 8) [*Tarantola*, 1987]. Through a large area of the model the velocity uncertainty is observed to be $< \pm 100$ ms^{-1}. East of the Peridotite Ridge there are lobes of higher velocity uncertainty, with the most prominent reaching $\pm$ ~150 ms^{-1} and corresponding to the high-velocity lobe directly below the S-reflector, between profile distances of 120 – 125 km. West of the Peridotite Ridge, a zone of low uncertainties ($< \pm 50$ ms^{-1}) between 30 – 75 km profile distance, underlies higher uncertainties ($\pm$ 50 – 100 ms^{-1}) at the top of the basement, and extending to depth between 75 – 85 km profile distance.

4.4.3 Checkerboard testing

Checkerboard tests (Figure 9) enable us to determine quantitatively the scale of resolvable structure in the final velocity model [*Zelt and Barton*, 1998]. Sinusoidal velocity perturbations of $\pm$ 5% were introduced in a checkerboard pattern to create reference models. Rays were traced through these reference models using a forward ray tracing method and the same shot-receiver geometry as the original inversion, producing synthetic travel times through each reference model. Random timing errors were added to these synthetic travel times, as described in the previous section, and were then inverted with the original model inputs and parameters [*Zhang and Toksöz*, 1998; *Korenaga et al.*, 2000]. The difference between these inversion results and the final velocity model were used to determine the length scale of structure resolved in the final velocity model.

Large-scale anomalies (25 km x 5 km) appear to be well resolved throughout the model at depths of 5 – 10 km, with the exception of the western and eastern limits, where the model is resolved by unidirectional ray paths. West of Peridotite Ridge (95 km profile distance), resolution below 10 km depth is poor for anomalies smaller than 25 km x 5 km, likely as a result of the limited ray coverage at this depth and the unidirectional rays from instrument 38

and 40. Anomalies below 10 km, east of the Peridotite Ridge, are recovered to a greater degree than those westward, but are not as well resolved as those at shallower depths. Small-scale anomalies (10 km x 2.5 km and 5 km x 2km) are well resolved throughout the model to depths of 10 km, with the exception of anomalies at 80 – 90 km profile distance, where a gap in the seismic profile has resulted in limited ray coverage in this region. Resolution of small-scale anomalies is excellent above the S-reflector, where ray coverage is densest, with the boundaries between tiles of opposite anomaly polarity exhibiting a reasonable match between the input and recovered velocity anomalies (Figure 7). The results of these checkerboard tests give confidence to the interpretation of large, basement scale velocity features west of the Peridotite Ridge, as well as the interpretation of smaller structures on the 5.0 x 2.5 km scale, associated with the S-reflector and continental hyperextension east of the Peridotite Ridge.

4.4 Moho reflections west of the Peridotite Ridge

Limited but clear reflected arrivals were observed at short offsets (mostly after the direct water arrival) in the receiver gathers of the four westernmost instruments (Figure 10), west of the Peridotite Ridge. One hundred clear PmP picks were identified from the receiver gathers of these four instruments (using an Ormsby band-pass filter of 1-2-20-40 Hz). In order to model the approximate depth of this interface, the PmP travel time picks were added to the travel time picks from modeling in section 4.3 and inverted with TOMO2D, using the same parameter set and input models. Locally, the same horizon which defined the initial S-reflector (7 km depth throughout the initial model) was adjusted in depth through the tomographic inversion, in order to match the modeled and observed PmP reflection travel times (Figure 10). An RMS misfit of 65 ms was achieved for these arrivals (Table 2).

These PmP arrivals are observed after basement reflections in the seismic receiver gathers (Figure 10), and must represent a velocity discontinuity. Such a discontinuity is not expected

within serpentinized mantle, and if it were a mid-crustal discontinuity, we would expect to see a Moho reflection beneath. Therefore we interpret these arrivals as reflections from the base of a thin crustal layer.

4.5 Gravity model

Conversion of the final velocity model to density, using empirical velocity-density (Vp-ρ) relationships, enables the calculation of the free-air gravity anomaly along the WE-1 profile [*Brocher*, 2005]. Comparison of this calculated anomaly with shipborne gravity observations permits validation of our velocity model, and can highlight areas where the model may be unreliable, or where there is significant out-of-plane structure. To avoid edge-effects, the velocity model was extended eastward, westward and to a depth of 25 km. The tomographic velocity model for the coincident ISE-1 seismic profile [*Zelt et al.*, 2003], was incorporated into our model and extends an additional ~250 km eastward (domain B, Figure 11). West of the WE-1 seismic profile there are no available geophysical or geological constraints, so the 1D velocity structure at 30 km model distance was extrapolated to -200 km (domain C, Figure 11). Mantle velocities (8.0 kms^{-1}) below the WE-1 model and domain C, were extended to 25 km depth in order to match the depth of the ISE-1 velocity model (domain D, Figure 11).

We used an assumed density of 1.03 g/cm^3 for the water column (< 1.55 kms^{-1}), and 3.30 g/cm^3 for the mantle (>= 8.0 kms^{-1}). Velocities within these bounds were converted to densities using the empirical Nafe-Drake relationship of *Ludwig et al.* [1970]. This relationship is most accurate when converting the compressional velocities of water saturated sediment to density, but also provides a good first order approximation of non-mantle rock densities [*Brocher*, 2005].

Free air gravity anomalies (FA) were calculated by summing the gravity anomaly of each model cell, approximated as an infinite cuboid out of plane, with a density contrast to a

439 background density of 3.3 g/cm^3 (Figure 11). A clear regional trend is observed in the
440 difference between the calculated and observed free air gravity anomaly, likely rising from
441 deeper mantle structures or assumptions made in creating the extended density model. To
442 correct for this regional trend, a linear trend was fit to this difference and subtracted from the
443 calculated free air gravity anomaly. This linear trend shows a decrease of 0.2 mGal/km
444 oceanward. Without this correction the model had a RMS misfit to the observed anomaly of
445 8.0 mGal, decreasing to 2.7 mGal after the trend removal, which is comparable to typical
446 shipborne gravity uncertainties [*Bell and Watts*, 1986]. Therefore gravity data provide further
447 support for our crustal velocity model.

448 # 5 Discussion

449 The final TOMO2D velocity model (Figure 5) enables the interpretation of many distinct
450 features including: the S-reflector east of the Peridotite Ridge; rotated and thinned continental
451 blocks topped with syn- and pre-rift sediment; thickening continental crust at the eastern end
452 of the WE-1 profile; the Peridotite Ridge, which reaches the seafloor in the center of the profile;
453 a relatively homogeneous basement west of the Peridotite Ridge; and a sparsely sampled Moho
454 interface at shallow depths. To investigate these features in greater detail, we divide the profile
455 into two parts bounded by the Peridotite Ridge.

456 ## 5.1 West of the Peridotite Ridge

457 ### 5.1.1 Velocity model and data features

458 Receiver gathers from the instruments west of the Peridotite Ridge bear a strong resemblance
459 to those from the IAM-9 seismic line, situated over the zone of exhumed continental mantle in
460 the southern Iberia Abyssal Plain [*Dean et al.*, 2000]. Apparent velocities > 7.0 kms^{-1} at short
461 offsets are indicative of mantle or serpentinized mantle at shallow depths, while a lack of deep
462 and clear PmP phase arrivals indicates the absence of full thickness oceanic crust (7 km thick)

along the profile. However, sparse Moho reflections identified after the direct arrival, on the four western most instruments, indicate the presence of an anomalously thin crust (Figure 10). We interpret this crust as oceanic because it appears highly magnetized [*Sibuet et al.*, 1995] and its seismic reflection characteristics differ markedly from those of thinned continental crust further east of the Peridotite Ridge [*Dean et al.*, 2015].

The final TOMO2D velocity model (Figure 5) shows that west of the Peridotite Ridge the basement velocity structure is relatively homogenous between 40 and 90 km model distance. There is slight variation in the velocities in what is interpreted as the top of basement, with lower velocities of 4.0 kms^{-1} at 30 – 52 km model distances, and higher velocities of 5.0 kms^{-1} at 55 – 75 km model distance. The 7.5 kms^{-1} velocity contour typically lies at round 12 km depth, but rises to shallower depths of 9 km and 10 km at profile distances of 40 km and 65 km, respectively. At the western limit of the model (< 30 km), velocity contours have a more uniform spread, and vary little from the input velocity model. Modeled PmP reflections reveal a thin oceanic layer that thickens seaward, from 0.5 km thick at 67 km profile distance, to 1.5 km thick at 36 km profile distance (Figure 10). No clear PmP arrival can be identified on instrument 78, which suggests that the oldest oceanic crust lies between instrument 76 and 78 (64 km and 83 km profile distance, respectively). Many of the seismic arrivals from this thin oceanic layer are masked by the direct water arrival and first arrivals from the shallow underlying mantle, and therefore cannot be resolved using first arrival travel times alone.

At its thinnest, the interpreted oceanic crustal layer has velocities between 4.5 and 5.5 kms^{-1}, and at its thickest has velocities between 4.0 and 6.5 kms^{-1}. Because the Moho velocity discontinuity has been smoothed out, these maximum velocities may be over-estimated. Velocities of 4.0 – 6.5 kms^{-1} are consistent with those commonly observed in oceanic layer 2 [*White et al.*, 1992]. Variations in the thickness of oceanic crust are commonly attributed to variations in the thickness of oceanic layer 3, while layer 2 typically remains constant [*Mutter*

488 *and Mutter*, 1993]. These observations lead us to conclude that oceanic layer 3 is absent in the
489 oceanic crust modeled along WE-1.

490 5.1.2 Velocity profiles

491 One-dimensional velocity profiles through the velocity model west of the Peridotite Ridge give
492 further insight into the nature of the unidentified basement (Figure 12). All of the 1-D velocity
493 profiles exhibit two distinct velocity trends, below the top of basement, which are identified
494 based on their common velocity gradients. The upper trend extends to depths of 2.8 - 3.5 km
495 below top basement. Velocities smoothly and rapidly increase from ~4.5 kms^{-1} to 7.3 – 7.6
496 kms^{-1} in this layer, and present velocity gradients ranging between 0.8 s^{-1} and 1.2 s^{-1}, with an
497 average velocity gradient of 1.0 s^{-1}. Despite Moho reflections being identified and modelled
498 within this depth range, no corresponding velocity discontinuity is present in our model,
499 because the TOMO2D inversion produces a smooth velocity model. Below this top trend,
500 compressional velocities smoothly increase toward mantle velocities of 8.0 kms^{-1}, and with a
501 much lower velocity gradient of 0.14 s^{-1} on average. These thicknesses and velocity gradients
502 are nearly identical to those observed by *Dean et al.* [2000] in the zone of exhumed continental
503 mantle in the southern Iberia Abyssal Plain, and are consistent with a decreasing
504 serpentinization of mantle material with depth [*Carlson and Miller*, 2003]. In our model, where
505 Moho reflections are not observed and exhumed mantle is interpreted (e.g., east of instrument
506 76, Figure 13), velocities of 4.6 kms^{-1} at the top of basement correspond to 100 %
507 serpentinization of mantle material, decreasing to < 20 % at depths of 2.8 – 3.5 km below top
508 basement [*Carlson and Miller*, 2003]. Velocities at depths > 2 km below the top basement sit
509 outside the envelope for all ages of Atlantic oceanic crust, but agree strongly with the velocities
510 observed within zones of transitional crust at both the southern Iberia Abyssal Plain and
511 Newfoundland margins (Figure 12). Velocities from our model also agree with the velocity
512 profiles through the models of thin oceanic crust, overlying serpentinized mantle, observed

along GP101 at the Deep Galicia margin, and SCREECH-1 at the conjugate Flemish Cap margin (Figure 12) [*Whitmarsh et al.,* 1996; *Funck et al.,* 2003; *Hopper et al.,* 2004]. These velocity models are derived by forward ray-tracing of seismic arrivals through discrete crustal layers, resulting in velocity jumps at layer boundaries, while our tomographic model produces a smooth velocity transition with depth. Seismic velocities reach 8 kms^{-1} corresponding to unaltered mantle material, at around 6 km below the top of basement in our model, which is consistent with other studies of exhumed and serpentinized peridotites at rifted margins (Figure 12).

From the velocity and seismic characteristics west of the Peridotite Ridge, we interpret that there is < 25 km of exhumed mantle (between the Peridotite Ridge and instrument 76, Figure 13), before the onset of thin oceanic crust overlying serpentinized mantle material. This thin oceanic layer thickens oceanward, but does not reach full thickness within our resolved velocity model. This interpretation is broadly consistent with previous interpretations of thin oceanic crust abutting the Peridotite Ridge and overlying serpentinized mantle [*Sibuet et al.*, 1995; *Whitmarsh et al.,* 1996]. However, *Whitmarsh et al.* [1996] used data from only three OBS along a 150-km-long margin-normal seismic profile and from three OBS along an 80-km-long margin-parallel profile. The authors from this study did not identify PmP arrivals from the base of the anomalously thin oceanic crust, while PmP arrivals from the base of full thickness oceanic crust (parallel to margin) were clearly identified only on one of the instruments west of the Peridotite Ridge. Our model shows a layer, identified by its constant velocity gradient, with a thickness of 2.8 – 3.5 km. This thickness is very similar to that of the thin oceanic crust described by *Whitmarsh et al.* [1996], and also correlates well with the layer of scattered reflectivity identified by *Dean et al.* [2015] (Figure 13). However, the base of this layer does not coincide with the Moho depths determined from limited PmP arrivals in our

model, and probably represents a change in the nature of mantle serpentinization below the thin oceanic crust.

Our interpretation of an anomalously thin oceanic crust is consistent with observations of thin oceanic crust at other ultra-slow spreading environments. Seismic refraction studies at the Gakkel Ridge (<10 mm/yr full spreading rate) have revealed oceanic crust 1.4 – 2.9 km thick, with little to no evidence of oceanic layer 3, overlying partially serpentinised mantle rock [*Jokat et al.*, 2003; *Jokat and Schmidt-Aursch*, 2007]. Wide-angle seismic data from the Southwest Indian Ridge (~12 mm/yr full spreading rate) suggest the presence of an oceanic crust which is 2.2 – 5.4 km thick, with serpentinised mantle rock proposed to comprise some of the oceanic layer 3 (0.5 – 3.0 km thick) [*Minshull et al.*, 2006]. Wide angle seismic studies of the Mohns Ridge (16 mm/yr full spreading rate) also revealed the presence of a thin oceanic crust ~4 km thick, with an oceanic layer 2 thickness of 1.4 – 1.7 km thick [*Klingelhöfer et al.*, 2000]. Our new data at the Deep Galicia margin contributes to the evidence that thin oceanic crust is the norm in ultra-slow spreading environments.

5.1.3 Reflection imaging

Dean et al. [2015] identify and describe the morphology of five ridge like basement structures in the reflection seismic images along WE-1 west of the Peridotite Ridge (indicated by R1 – R4 in Figure 13). Unlike the reflection imaging of continental crust east of the Peridotite Ridge, west of the Peridotite Ridge the reflection data exhibits scattered reflectivity and a diminished presence of coherent structural reflections within the basement. Ridges 1 – 3a exhibit an asymmetric structure with limited elevation above the surrounding basement topography, have little internal structure, and smooth to sub-angular basement expression. Ridges 3b and 4 are symmetric in structure, with smooth surfaces that rise high above the surrounding basement topography. The rough, or hummocky, morphology of ridges 1 – 3a is consistent with the

accretion of magmatic crust at ultra-slow spreading ridges, such as that seen along sections of the Southwest Indian Ridge [*Cannat et al.,* 2006]. Conversely, smooth basement ridge structures, like that of ridges 3b and 4, are also observed in areas of the Southwest Indian Ridge, and are interpreted to be the exhumation and exposure of altered mantle-derived rocks [*Cannat et al.*, 2006]. *Dean et al.* [2015] proposed a synthesis model for the generation of these ridges, suggesting that ridges 1 - 3a were formed through mantle exhumation and interspersed magmatism, while ridge 4 resembles an oceanic core complex (OCC). Our results support the interpretation of ridges 1 – 3a as magmatic in origin, and that this magmatic layer overlies serpentinized mantle. High P-wave velocities are expected at shallow depths in oceanic core complexes, due to presence of gabbro or ultramafic material (~6.0 kms^{-1} and >7.5 kms^{-1}, respectively) [*Blackman et al.,* 2009]. Velocity modeling of OCC at the Atlantis Platform on the Southwest Indian Ridge, revealed P-wave velocities of 5.8 kms^{-1} at the seafloor, increasing to 6.5 kms^{-1} at 1.4 km depth [*Muller et al.,* 2000]; at the Parece Vela Basin, in the Philippine Sea, P-wave velocities of 6.0 kms^{-1} were modeled at depths of 500 m [*Ohara et al.*, 2007]; at 26°N along the Mid-Atlantic Ridge P-wave velocities are modeled as 4.0 kms^{-1} at the seafloor, increasing to 7.0 kms^{-1} within 1 km below [*Canales et al.*, 2007; *Sohn et al.,* 2007]. These velocity structures are markedly different to that resolved at ridge 4 along WE-1, where P-wave velocities increase from 4.0 kms^{-1} at the seafloor, to 6.0 kms^{-1} (i.e.: seismic velocity of gabbro) ~2.7 km below, which is significantly deeper than the previously described OCC. Therefore, our data do not support the interpretation that this ridge is an oceanic core complex. We suggest that all of these ridge features are formed through magma-limited accretion of thin oceanic crust.

5.1.4 Conjugate margin

Thin oceanic crust is also observed on the SCREECH-1 profile at the Flemish Cap, which in many reconstructions is conjugate to both WE-1 and ISE-1. Magmatic crust, 3-4 km thick, is

586 interpreted to have been accreted in direct contact with the termination of extended continental
587 crust, defining a sharp COT [*Hopper et al.*, 2004]. This initial oceanic crust is highly faulted,
588 with rotated fault blocks, bound by normal faults dipping seaward every ~1.5 km. Further
589 seaward, oceanic crust becomes extremely thin (~1.3 km thick) and is underlain by
590 serpentinized mantle, much like the thin oceanic crust which we have interpreted at the Deep
591 Galicia margin. In the reflection seismic images of WE-1 (Figure 13) and its interpretation west
592 of the Peridotite Ridge, block-bounding faults, similar to those observed along SCREECH-1,
593 are not imaged [*Hopper et al.*, 2004]. Such faults may be present, but sub seismic in nature and
594 unresolved in the Kirchhoff time migration images (Figure 13). Such faulting would provide
595 the required mechanism to hydrate, and consequently enable the serpentinization, of the
596 underlying mantle. Additionally, in the seismic reflection images, there is little evidence for a
597 strong and coherent Moho reflection from the base of the thin oceanic crust, which is evidence
598 in support of a weak velocity contrast across this boundary.

599 5.1.5 Dating the earliest oceanic crust

600 A lack of linear seafloor spreading magnetic anomalies and drill sites, west of the Peridotite
601 Ridge, make it difficult to assign an age to the earliest oceanic crust seen at the Deep Galicia
602 margin. *Srivastava et al.* [2000] interpret a magnetic anomaly, west of the Peridotite Ridge, as
603 spreading anomaly M0 (~126 Ma, according to timescale of *Gradstein et al.* [2012]) (Figures
604 10 and 13). However, caution must be applied to this interpretation, as *Sibuet et al.* [1995] fit
605 a model to the same magnetic data, showing that the topography of a highly magnetized (5
606 A/m), and thin oceanic crust (~1 km), recording no magnetic field reversals, can also explain
607 the observed magnetic anomaly. *Sibuet et al.* [1995] also state that no magnetic field reversals
608 were expected, as oceanic crust in this region formed during the Cretaceous constant polarity
609 interval, later than the M series of seafloor spreading magnetic anomalies. Age constraints
610 could alternatively come from the drilling of the Peridotite Ridge, which was sampled by site

637 of IODP Leg 173 (Figure 1C), and returned serpentinized mantle peridotite intruded with amphibole-diorites, gabbros and pyroxenites [*Boillot et al.*, 1987]. Dating of samples from Site 637, and other drill and dive sites along the deep Galicia margin, show that the mafic rocks were emplaced at around 122 Ma, synchronous with the end of rifting [*Schärer et al.*, 1995; *Chazot et al.*, 2005]. This date is younger than that of the M0 magnetic anomaly, and suggests an upper bound to the age of oceanic crust west of the Peridotite Ridge of 122 Ma. This date also enables us to estimate a spreading rate for the accretion of this oceanic crust. Site 637 is approximately 280 km from the nearest magnetic isochron (C34), which is the first clear seafloor spreading magnetic anomaly after the Cretaceous constant polarity interval, and has an age of 84 Ma [*Bronner et al.*, 2011; *Gradstein et al.*, 2012]. The required half spreading rate is 7.4 mm/yr, classifying the spreading here as ultra-slow, which is consistent with the observed mantle exhumation and onset of thin oceanic crust. South of the Deep Galicia margin, at the southern Iberia Abyssal Plain, the formation of oceanic crust 6 - 7 km thick is interpreted to have begun at 127 – 125 Ma, while north of the Deep Galicia margin, at the Goban Spur, a final breakup age of 100 Ma is proposed [*Gerlings et al.*, 2012; *Minshull et al.*, 2014]. These breakup dates, decreasing in age from south to north, are consistent with the observation of a northward propagating rift margin [*Masson and Miles*, 1984]. At the Flemish Cap, conjugate to the Deep Galicia margin, oceanic crust is observed to have accreted just after M0 magnetic anomaly along SCREECH-1, at around 123.5 Ma, which is consistent with our interpretation [*Hopper et al.*, 2004; *Van Avendonk et al.*, 2006].

5.2 East of the Peridotite Ridge

5.2.1 Comparison with existing models

Inversion of the WE-1 wide-angle seismic dataset has yielded a velocity model east of the Peridotite Ridge which strongly correlates with the structure observed in reflection imaging

635 and the classical interpretations of the hyperextended Deep Galicia margin (Figure 14C).
636 Additional to the velocity model developed in this study, two coincident compressional
637 velocity models have previously been produced east of the Peridotite Ridge (Figure 14). All
638 three models have been developed using different modeling techniques. The preferred model
639 of *Zelt et al.* [2003] (Figure 14A) was developed using wide-angle and zero-offset MCS picks,
640 from the ISE-1 profiled, inverted simultaneously using the *Zelt and Smith* [1992] algorithm.
641 This model utilized a priori information by defining a six-layer starting model including the
642 water column, three sedimentary layers, a crustal layer and a mantle layer, constrained by MCS
643 imaging along the ISE-1 seismic line. The model of *Bayrakci et al.* [2016] (Figure 14B) is a
644 two-dimensional slice, coincident with WE-1 and ISE-1, of a larger three-dimensional
645 compressional velocity model developed using data from the full array of instruments within
646 the 3D box of the Galicia-3D seismic experiment (see Section 3). This three-dimensional
647 velocity model was developed using first arrival seismic travel times, inverted using a non-
648 linear iterative tomographic technique (FAST) [*Zelt and Barton*, 1998]. In the following
649 description of the structure east of the Peridotite Ridge, we primarily describe the results of our
650 tomographic modeling, with comparison to those of *Zelt et al.* [2003] and *Bayrakci et al.*
651 [2016], which we will refer to as the ISE and G3D models, respectively.

652 Velocities in the rotated continental fault blocks, bound by normal faults (illustrated as F3-F7
653 in Figure 13), and the pre- and syn-rift sedimentary layers above, appear to have been well
654 resolved. The velocity structure exhibits landward dipping contours, but due to model
655 limitations, cannot match the steep boundaries interpreted between pre-rift sediment, syn-rift
656 sediment, and crystalline crust layers. The tops of the fault-bounded blocks are better defined
657 at shallow depths than in the G3D velocity model, owing to finer model cells at shallow depths
658 in our model when compared to the G3D model, and the a priori information used in the WE-1
659 input model. Velocities increase from ~3.0 kms^{-1} at the top of syn-rift sediment, to ~4.5 kms^{-1}

660 at the top of pre-rift sediment, and to ~6.5 kms^{-1} at the base of crystalline crust, directly above
661 the S-reflector. The S-reflector follows the 6.0 – 7.0 kms^{-1} velocity contours between profile
662 distances of 112 – 135 km, and has an excellent match with the interpretations of depth-
663 migrated multi-seismic along GP12 and ISE-1 [*Reston et al.*, 1996; *Borgmeyer*, 2010], as well
664 as the G3D velocity model. These velocities are interpreted to correspond to ~30 – 60 %
665 serpentinization of mantle peridotite [*Carlson and Miller*, 2003]. At its eastern limit (> 132 km)
666 the S-reflector cuts through lower seismic velocities associated with the continental crust,
667 before terminating at the seafloor at ~147.5 km profile distance. The western limit of the S-
668 reflector shallows toward the Peridotite Ridge, before terminating at 112 km.

669 The S-reflector exhibits undulations along profile in our tomography model, which have a
670 moderate correlation with the rotated continental fault blocks juxtaposed above this detachment
671 surface in both our velocity model and the G3D velocity model. It is possible that smoothing
672 in the velocity model has resulted in seismic pull-up and/or push-down, which is observed as
673 the undulations in the resolved S-reflector. Below the S-reflector a pattern of high and low-
674 velocity regions are observed. The most prominent high-velocity region observed below the
675 S-reflector reaches 8.0 kms^{-1}, 100 m below the S-reflector at 122 km profile distance, rapidly
676 decreasing eastward to a zone with a velocity of 6.5 kms^{-1} at 128 km profile distance, before
677 again increasing to 7.2 kms^{-1} at 132 km profile distance. These velocities are interpreted to
678 correspond to different degrees of serpentinization of the mantle peridotite along the
679 S-reflector, with 8.0 kms^{-1} being unaltered, 6.4 kms^{-1} indicating ~45 % serpentinization and
680 7.2 kms^{-1} representing ~20 % serpentinization [*Carlson and Miller*, 2003]. The 6.5 kms^{-1}
681 velocity zone occurs between normal faults marked as F5 and F4, and we propose that this low-
682 velocity zone the result of fluid transport along fault F4, resulting in the pattern of variable
683 hydration and serpentinization of the upper mantle along the S-reflector [*Bayrakci et al.*, 2016].
684 However, the high-velocity lobe situated at the terminus of fault F5 is problematic for this

interpretation. Movement along the S-detachment could have shifted this low-velocity zone laterally eastward, but this contradicts the idea that the velocity variation below the S-reflector is a result of preferential mantle hydration by fault fluid transport, which occurs when the faults are displaced. However, the G3D velocity model shows an offset in these high and low-velocity patterns, when compared with the velocity model from this study, with the low-velocity lobes situated down-dip of the terminus of normal faults, giving strong evidence in favor of fault controlled mantle hydration [*Bayrakci et al.*, 2016]. The difference in the models could be explained by the more complete azimuthal coverage of the G3D velocity model, enabling this structure to be resolved in the third dimension, where our 2D model is unable to do so. The Monte Carlo uncertainty results also shows that the uncertainty of this structure in our model is highest throughout the model, reaching ± 0.15 kms^{-1} (Figure 8). In contrast, the S-reflector is modeled as a seaward dipping interface, free of undulations, in the lower-resolution ISE velocity model.

The velocity within the Peridotite Ridge reaches a maximum of ~8.0 kms^{-1} in both the model from this study and the G3D model, indicating the presence of unaltered mantle peridotite at the center of the Peridotite Ridge. This is a much higher velocity than modeled in the ISE model, where the maximum velocity is 6.0 – 6.5 kms^{-1}. However, the velocities in our model and the G3D model form closed-contour high-velocity blobs, with lower velocities below the Peridotite Ridge, which is difficult to interpret.

At the eastern limit of the ISE model, the Moho is modeled as an abrupt velocity jump from 7 kms^{-1} to 8 kms^{-1} across a landward dipping horizon. The Moho is not included as a layer boundary in our tomographic model, or the G3D model, so such an abrupt velocity jump is not possible in the tomography model of this study and that of the G3D study. However, the 7 kms^{-1} velocity contour of both models show a strong correlation with the Moho modeled in the ISE model.

6 Conclusions

Our final compressional velocity model has resolved the structure of continental hyperextension, detachment faulting, the Peridotite Ridge, and a thin oceanic crust overlying serpentinized mantle material. There is a strong correlation between the structure resolved in our velocity model and that observed in coincident seismic reflection data. The final model is further validated by the close fit between the observed and calculated free-air gravity anomaly. The primary findings from this study are as follows:

1. West of the Peridotite Ridge, exhumed mantle is present over a short distance (< 25 km), landward of the onset of an anomalously thin oceanic crust (0.5 – 1.5 km thick), which thickens seaward. Evidence for the presence of serpentinized mantle material below this thin oceanic crust comes from seismic velocities increasing smoothly from 5.5 – 6.5 km s^{-1} to 7.3 – 7.6 km s^{-1}, with a velocity gradient of 1.0 s^{-1}. Below this, velocities increase slowly into mantle velocities of ~8.0 kms^{-1}, with an average velocity gradient of ~0.14 s^{-1}.
2. We assign an upper bound to the age of the thin oceanic crust of 122 Ma, based on the dating of materials recovered from the Peridotite Ridge. This age is consistent with continental breakup progressing from south to north along the margin.
3. The S-reflector detachment surface possesses undulations that correlate with the pattern of high and low-velocity regions below this surface. This velocity structure is interpreted to be the result of preferential mantle hydration along normal faults, acting as conduits between the seafloor and the S-reflector. Typically the S-reflector lies between the 6.0 and 7.0 kms^{-1} velocity contours, which corresponds to serpentinization of mantle peridotite of 60 – 30%, respectively.

7 Acknowledgments

This research was supported by the US National Science Foundation, the UK Natural Environment Research Council and GEOMAR Helmholtz Centre for Ocean Research. The NERC grant code for this project is NE/E016502/1. T.A.M. was supported by a Wolfson Research Merit award. Ocean bottom instrumentation was provided by the UK Ocean Bottom Instrumentation Facility and by GEOMAR. We would like to thank everyone who participated and contributed hard work to the data acquisition, either aboard the R/V Marcus Langseth or the F/S Poseidon We would also like to thank the reviewers, Harm Van Avendonk, Kim Welford and an anonymous reviewer, as well as the associate editor, Mladen Nedimović, for their valuable feedback on the manuscript. The wide angle seismic data used in this study can be accessed at https://doi.pangaea.de/10.1594/PANGAEA.859069 (WE-1) and http://www-udc.ig.utexas.edu/sdc/cruise.php?cruiseIn=ew9705 (ISE-1).

8 References

Bayrakci, G., et al. (2016), Fault-controlled hydration of the upper mantle during continental rifting, *Nature Geosci*, *advance online publication*, doi:10.1038/ngeo2671.

Bell, R. E., and A. B. Watts (1986), Evaluation of the BGM-3 sea gravity meter system onboard R/V Conrad, *Geophysics*, *51*(7), 1480-1493.

Beslier, M.-O., M. Ask, and G. Boillot (1993), Ocean-continent boundary in the Iberia Abyssal Plain from multichannel seismic data, *Tectonophysics*, *218*(4), 383-393.

Blackman, D. K., J. P. Canales, and A. Harding (2009), Geophysical signatures of oceanic core complexes, *Geophysical Journal International*, *178*(2), 593-613.

Blackman, D. K., J. A. Karson, D. S. Kelley, J. R. Cann, G. L. Früh-Green, J. S. Gee, S. D. Hurst, B. E. John, J. Morgan, and S. L. Nooner (2002), Geology of the Atlantis Massif (Mid-Atlantic Ridge, 30 N): Implications for the evolution of an ultramafic oceanic core complex, *Marine Geophysical Researches*, *23*(5-6), 443-469.

Boillot, G., E. Winterer, and A. Meyer (1987), Introduction, objectives, and principal results: Ocean Drilling Program Leg 103, west Galicia Margin, paper presented at Proc. Ocean Drill. Program, Initial Reports.

Borgmeyer, A. L. (2010), Three-dimensional geometries of rifting on a hyperextended margin-Interpretation of seismic reflection profiles from the Deep Galicia Basin, Iberia, MSc thesis, RICE University.

Bown, J. W., and R. S. White (1995), Effect of finite extension rate on melt generation at rifted continental margins, *Journal of Geophysical Research: Solid Earth (1978–2012)*, *100*(B9), 18011-18029.

Brocher, T. M. (2005), Empirical relations between elastic wavespeeds and density in the Earth's crust, *Bulletin of the Seismological Society of America*, *95*(6), 2081-2092.

Bronner, A., D. Sauter, G. Manatschal, G. Péron-Pinvidic, and M. Munschy (2011), Magmatic breakup as an explanation for magnetic anomalies at magma-poor rifted margins, *Nature Geoscience*, *4*(8), 549-553.
Buck, W. R. (1991), Modes of continental lithospheric extension, *Journal of Geophysical Research: Solid Earth (1978–2012)*, *96*(B12), 20161-20178.
Canales, J. P., R. A. Sohn, and B. J. Demartin (2007), Crustal structure of the Trans-Atlantic Geotraverse (TAG) segment (Mid-Atlantic Ridge, 26° 10′ N): Implications for the nature of hydrothermal circulation and detachment faulting at slow spreading ridges, *Geochemistry, Geophysics, Geosystems*, *8*(8).
Cannat, M., D. Sauter, V. Mendel, E. Ruellan, K. Okino, J. Escartin, V. Combier, and M. Baala (2006), Modes of seafloor generation at a melt-poor ultraslow-spreading ridge, *Geology*, *34*(7), 605-608.
Carlson, R. L., and D. J. Miller (2003), Mantle wedge water contents estimated from seismic velocities in partially serpentinized peridotites, *Geophysical Research Letters*, *30*(5).
Chazot, G., S. Charpentier, J. Kornprobst, R. Vannucci, and B. Luais (2005), Lithospheric mantle evolution during continental break-up: the West Iberia non-volcanic passive margin, *Journal of Petrology*, *46*(12), 2527-2568.
Chian, D., K. E. Louden, T. A. Minshull, and R. B. Whitmarsh (1999), Deep structure of the ocean-continent transition in the southern Iberia Abyssal Plain from seismic refraction profiles: Ocean Drilling Program (Legs 149 and 173) transect, *Journal of Geophysical Research: Solid Earth (1978–2012)*, *104*(B4), 7443-7462.
Christensen, N. I. (2004), Serpentinites, peridotites, and seismology, *International Geology Review*, *46*(9), 795-816.
Dean, S., T. Minshull, R. Whitmarsh, and K. Louden (2000), Deep structure of the ocean-continent transition in the southern Iberia Abyssal Plain from seismic refraction profiles: The IAM-9 transect at 40 20′ N, *Journal of Geophysical Research: Solid Earth (1978–2012)*, *105*(B3), 5859-5885.
Dean, S., D. Sawyer, and J. Morgan (2015), Galicia Bank ocean–continent transition zone: New seismic reflection constraints, *Earth and Planetary Science Letters*, *413*, 197-207.
Funck, T., J. R. Hopper, H. C. Larsen, K. E. Louden, B. E. Tucholke, and W. S. Holbrook (2003), Crustal structure of the ocean-continent transition at Flemish Cap: Seismic refraction results, *Journal of Geophysical Research: Solid Earth*, *108*(B11), n/a-n/a, doi:10.1029/2003JB002434.
Gerlings, J., K. E. Louden, T. A. Minshull, and M. R. Nedimović (2012), Flemish Cap–Goban Spur conjugate margins: new evidence of asymmetry, *Geology*, *40*(12), 1107-1110.
Gradstein, F. M., J. G. Ogg, M. Schmitz, and G. Ogg (2012), *The Geologic Time Scale 2012 2-Volume Set*, elsevier.
Granot, R., J. Dyment, and Y. Gallet (2012), Geomagnetic field variability during the Cretaceous Normal Superchron, *Nature Geoscience*, *5*(3), 220-223.
Hopper, J. R., T. Funck, B. E. Tucholke, H. C. Larsen, W. S. Holbrook, K. E. Louden, D. Shillington, and H. Lau (2004), Continental breakup and the onset of ultraslow seafloor spreading off Flemish Cap on the Newfoundland rifted margin, *Geology*, *32*(1), 93-96.
Jokat, W., O. Ritzmann, M. C. Schmidt-Aursch, S. Drachev, S. Gauger, and J. Snow (2003), Geophysical evidence for reduced melt production on the Arctic ultraslow Gakkel mid-ocean ridge, *Nature*, *423*(6943), 962-965.
Jokat, W., and M. C. Schmidt-Aursch (2007), Geophysical characteristics of the ultraslow spreading Gakkel Ridge, Arctic Ocean, *Geophysical journal international*, *168*(3), 983-998.
Klingelhöfer, F., L. Geli, L. Matias, N. Steinsland, and J. Mohr (2000), Crustal structure of a super-slow spreading centre: a seismic refraction study of Mohns Ridge, 72 N, *Geophysical Journal International*, *141*(2), 509-526.
Klitgord, K., and H. Schouten (1986), Plate kinematics of the central Atlantic, *The Geology of North America*, *1000*, 351-378.
Korenaga, J., W. Holbrook, G. Kent, P. Kelemen, R. Detrick, H. C. Larsen, J. Hopper, and T. Dahl-Jensen (2000), Crustal structure of the southeast Greenland margin from joint refraction and

reflection seismic tomography, *Journal of Geophysical Research: Solid Earth (1978–2012)*, *105*(B9), 21591-21614.
Lavier, L. L., and G. Manatschal (2006), A mechanism to thin the continental lithosphere at magma-poor margins, *Nature*, *440*(7082), 324-328.
Ludwig, W. J., J. E. Nafe, and C. L. Drake (1970), Seismic refraction, *The sea*, *4*(Part 1), 53-84.
Masson, D., and P. Miles (1984), Mesozoic seafloor spreading between Iberia, Europe and North America, *Marine Geology*, *56*(1), 279-287.
Maus, S., U. Barckhausen, H. Berkenbosch, N. Bournas, J. Brozena, V. Childers, F. Dostaler, J. Fairhead, C. Finn, and R. Von Frese (2009), EMAG2: A 2–arc min resolution Earth Magnetic Anomaly Grid compiled from satellite, airborne, and marine magnetic measurements, *Geochemistry, Geophysics, Geosystems*, *10*(8).
Minshull, T., S. Dean, R. White, and R. Whitmarsh (2001), Anomalous melt production after continental break-up in the southern Iberia Abyssal Plain, *Geological Society, London, Special Publications*, *187*(1), 537-550.
Minshull, T., S. Dean, and R. Whitmarsh (2014), The peridotite ridge province in the southern Iberia Abyssal Plain: Seismic constraints revisited, *Journal of Geophysical Research: Solid Earth*, *119*(3), 1580-1598.
Minshull, T., M. Muller, and R. White (2006), Crustal structure of the Southwest Indian Ridge at 66 E: Seismic constraints, *Geophysical Journal International*, *166*(1), 135-147.
Minshull, T. A. (2009), Geophysical characterisation of the ocean–continent transition at magma-poor rifted margins, *Comptes Rendus Geoscience*, *341*(5), 382-393.
Minshull, T. A., M. C. Sinha, and C. Peirce (2005), Multi-disciplinary, sub-seabed geophysical imaging, *Sea Technology*, *46*(10), 27-31.
Mohn, G., G. D. Karner, G. Manatschal, and C. A. Johnson (2015), Structural and stratigraphic evolution of the Iberia–Newfoundland hyper-extended rifted margin: a quantitative modelling approach, *Geological Society, London, Special Publications*, *413*, SP413. 419.
Muller, M., T. Minshull, and R. White (2000), Crustal structure of the Southwest Indian Ridge at the Atlantis II fracture zone, *Journal of Geophysical Research: Solid Earth*, *105*(B11), 25809-25828.
Murillas, J., D. Mougenot, G. Boulot, M. Comas, E. Banda, and A. Mauffret (1990), Structure and evolution of the Galicia Interior Basin (Atlantic western Iberian continental margin), *Tectonophysics*, *184*(3), 297-319.
Mutter, C. Z., and J. C. Mutter (1993), Variations in thickness of layer 3 dominate oceanic crustal structure, *Earth and Planetary Science Letters*, *117*(1), 295-317.
Ohara, Y., K. Okino, and J. Kasahara (2007), Seismic study on oceanic core complexes in the Parece Vela back-arc basin, *Island Arc*, *16*(3), 348-360.
Pérez-Gussinyé, M. (2013), A tectonic model for hyperextension at magma-poor rifted margins: an example from the West Iberia–Newfoundland conjugate margins, *Geological Society, London, Special Publications*, *369*(1), 403-427.
Pérez-Gussinyé, M., J. P. Morgan, T. J. Reston, and C. R. Ranero (2006), The rift to drift transition at non-volcanic margins: insights from numerical modelling, *Earth and Planetary Science Letters*, *244*(1), 458-473.
Pérez-Gussinyé, M., C. Ranero, T. J. Reston, and D. Sawyer (2003), Mechanisms of extension at nonvolcanic margins: Evidence from the Galicia interior basin, west of Iberia, *Journal of Geophysical Research: Solid Earth (1978–2012)*, *108*(B5).
Pérez-Gussinyé, M., and T. J. Reston (2001), Rheological evolution during extension at nonvolcanic rifted margins: onset of serpentinization and development of detachments leading to continental breakup, *Journal of Geophysical Research: Solid Earth (1978–2012)*, *106*(B3), 3961-3975.
Peron-Pinvidic, G., G. Manatschal, and P. T. Osmundsen (2013), Structural comparison of archetypal Atlantic rifted margins: a review of observations and concepts, *Marine and Petroleum Geology*, *43*, 21-47.

Péron-Pinvidic, G., G. Manatschal, T. A. Minshull, and D. S. Sawyer (2007), Tectonosedimentary evolution of the deep Iberia-Newfoundland margins: Evidence for a complex breakup history, *Tectonics*, *26*(2).
Pickup, S., R. Whitmarsh, C. Fowler, and T. Reston (1996), Insight into the nature of the ocean-continent transition off West Iberia from a deep multichannel seismic reflection profile, *Geology*, *24*(12), 1079-1082.
Ranero, C. R., and M. Pérez-Gussinyé (2010), Sequential faulting explains the asymmetry and extension discrepancy of conjugate margins, *Nature*, *468*(7321), 294-299.
Reston, T. (2007a), Extension discrepancy at North Atlantic nonvolcanic rifted margins: Depth-dependent stretching or unrecognized faulting?, *Geology*, *35*(4), 367-370.
Reston, T. (2009), The structure, evolution and symmetry of the magma-poor rifted margins of the North and Central Atlantic: a synthesis, *Tectonophysics*, *468*(1), 6-27.
Reston, T., C. Krawczyk, and D. Klaeschen (1996), The S reflector west of Galicia (Spain): Evidence from prestack depth migration for detachment faulting during continental breakup, *Journal of Geophysical Research: Solid Earth (1978–2012)*, *101*(B4), 8075-8091.
Reston, T., and K. McDermott (2014), An assessment of the cause of the 'extension discrepancy'with reference to the west Galicia margin, *Basin Research*, *26*(1), 135-153.
Reston, T. J. (2007b), The formation of non-volcanic rifted margins by the progressive extension of the lithosphere: the example of the West Iberian margin, *Geological Society, London, Special Publications*, *282*(1), 77-110.
Reston, T. J. (2010), The opening of the central segment of the South Atlantic: symmetry and the extension discrepancy, *Petroleum Geoscience*, *16*(3), 199-206.
Reston, T. J., T. Leythäuser, G. Booth-Rea, D. Sawyer, D. Klaeschen, and C. Long (2007), Movement along a low-angle normal fault: The S reflector west of Spain, *Geochemistry, Geophysics, Geosystems*, *8*(6).
Russell, S., and R. Whitmarsh (2003), Magmatism at the west Iberia non-volcanic rifted continental margin: evidence from analyses of magnetic anomalies, *Geophysical Journal International*, *154*(3), 706-730.
Sallarès, V., A. Gailler, M.-A. Gutscher, D. Graindorge, R. Bartolomé, E. Gracia, J. Diaz, J. J. Dañobeitia, and N. Zitellini (2011), Seismic evidence for the presence of Jurassic oceanic crust in the central Gulf of Cadiz (SW Iberian margin), *Earth and Planetary Science Letters*, *311*(1), 112-123.
Sawyer, D., R. Whitmarsh, and A. Klaus (1994), Iberia Abyssal Plain Sites 897-901, paper presented at Proceedings of the ocean drilling program initial reports.
Sawyer, D. S., T. Reston, M. P. Gussinye, C. A. Zelt, J. A. Austin, Y. Nakamura, J. Danobeitia, C. D., and S. P. o. E. C. 97-05 (1997), The Iberia Seismic Experiment (ISE97): MCS reflection profiles, *EOS*, *78*(F468).
Schärer, U., J. Kornprobst, M.-O. Beslier, G. Boillot, and J. Girardeau (1995), Gabbro and related rock emplacement beneath rifting continental crust: U Pb geochronological and geochemical constraints for the Galicia passive margin (Spain), *Earth and Planetary Science Letters*, *130*(1), 187-200.
Shillington, D. J., W. S. Holbrook, H. J. Van Avendonk, B. E. Tucholke, J. R. Hopper, K. E. Louden, H. C. Larsen, and G. T. Nunes (2006), Evidence for asymmetric nonvolcanic rifting and slow incipient oceanic accretion from seismic reflection data on the Newfoundland margin, *Journal of Geophysical Research: Solid Earth (1978–2012)*, *111*(B9).
Sibuet, J.-C., V. Louvel, R. B. Whitmarsh, R. S. White, S. J. Horsefield, B. Sichler, P. Léon, and M. Recq (1995), Constraints on rifting processes from refraction and deep-tow magnetic data: the example of the Galicia continental margin (West Iberia), in *Rifted ocean-continent boundaries*, edited, pp. 197-217, Springer.
Sibuet, J. C., S. Srivastava, and G. Manatschal (2007), Exhumed mantle-forming transitional crust in the Newfoundland-Iberia rift and associated magnetic anomalies, *Journal of Geophysical Research: Solid Earth (1978–2012)*, *112*(B6).

921 Sohn, R. A., J. P. Canales, and S. E. Humphris (2007), Kinematics and geometry of active detachment
922 faulting beneath the Trans-Atlantic Geotraverse (TAG) hydrothermal field on the Mid-Atlantic Ridge,
923 *Geology*, *35*(8), 711-714.
924 Srivastava, S., J.-C. Sibuet, S. Cande, W. Roest, and I. D. Reid (2000), Magnetic evidence for slow
925 seafloor spreading during the formation of the Newfoundland and Iberian margins, *Earth and*
926 *Planetary Science Letters*, *182*(1), 61-76.
927 Tarantola, A. (1987), Inverse Problem Theory: Models for Data Fitting and Model Parameter
928 Estimation, 613 pp, edited, Elsevier Sci., New York.
929 Tucholke, B., D. Sawyer, and J.-C. Sibuet (2007), Breakup of the Newfoundland–Iberia rift, *Geological*
930 *Society, London, Special Publications*, *282*(1), 9-46.
931 Tucholke, B., J. Sibuet, and A. Klaus (2004), 1. Leg 210 Summary, paper presented at Proc. Ocean
932 Drill. Program, Initial Rep.
933 Tucholke, B. E., and J.-C. Sibuet (2007), Leg 210 synthesis: tectonic, magmatic, and sedimentary
934 evolution of the Newfoundland-Iberia rift, paper presented at Proceedings of the Ocean Drilling
935 Program, scientific results.
936 Van Avendonk, H. J., W. S. Holbrook, G. T. Nunes, D. J. Shillington, B. E. Tucholke, K. E. Louden, H. C.
937 Larsen, and J. R. Hopper (2006), Seismic velocity structure of the rifted margin of the eastern Grand
938 Banks of Newfoundland, Canada, *Journal of Geophysical Research: Solid Earth (1978–2012)*,
939 *111*(B11).
940 Van Avendonk, H. J., L. L. Lavier, D. J. Shillington, and G. Manatschal (2009), Extension of continental
941 crust at the margin of the eastern Grand Banks, Newfoundland, *Tectonophysics*, *468*(1), 131-148.
942 White, R. S., D. McKenzie, and R. K. O'Nions (1992), Oceanic crustal thickness from seismic
943 measurements and rare earth element inversions, *Journal of Geophysical Research: Solid Earth*
944 *(1978–2012)*, *97*(B13), 19683-19715.
945 Whitmarsh, R., M. Beslier, and P. Wallace (1998), Leg 173, paper presented at Proc. ODP, Init. Rep.
946 Whitmarsh, R., G. Manatschal, and T. Minshull (2001a), Evolution of magma-poor continental
947 margins from rifting to seafloor spreading, *Nature*, *413*(6852), 150-154.
948 Whitmarsh, R. B., and P. R. Miles (1995), Models of the development of the West Iberia rifted
949 continental margin at 40° 30′ N deduced from surface and deep-tow magnetic anomalies, *Journal of*
950 *Geophysical Research: Solid Earth (1978–2012)*, *100*(B3), 3789-3806.
951 Whitmarsh, R. B., P. J. Wallace, and M.-O. Beslier (2001b), The rift-to-drift development of the west
952 Iberia nonvolcanic continental margin: a summary and review of the contribution of Ocean Drilling
953 Program Leg 173, *Proceedings of the Ocean Drilling Program, Scientific Results, 173*, 36-36.
954 Whitmarsh, R. B., R. S. White, S. J. Horsefield, J. C. Sibuet, M. Recq, and V. Louvel (1996), The ocean-
955 continent boundary off the western continental margin of Iberia: Crustal structure west of Galicia
956 Bank, *Journal of Geophysical Research: Solid Earth (1978–2012)*, *101*(B12), 28291-28314.
957 Xu, M., J. P. Canales, B. E. Tucholke, and D. L. DuBois (2009), Heterogeneous seismic velocity
958 structure of the upper lithosphere at Kane oceanic core complex, Mid-Atlantic Ridge, *Geochemistry,*
959 *Geophysics, Geosystems*, *10*(10).
960 Zelt, C., and R. Smith (1992), Seismic traveltime inversion for 2-D crustal velocity structure,
961 *Geophysical journal international*, *108*(1), 16-34.
962 Zelt, C. A., and P. J. Barton (1998), Three-dimensional seismic refraction tomography: A comparison
963 of two methods applied to data from the Faeroe Basin, *Journal of Geophysical Research: Solid Earth*
964 *(1978–2012)*, *103*(B4), 7187-7210.
965 Zelt, C. A., K. Sain, J. V. Naumenko, and D. S. Sawyer (2003), Assessment of crustal velocity models
966 using seismic refraction and reflection tomography, *Geophysical Journal International*, *153*(3), 609-
967 626.
968 Zhang, J., and M. N. Toksöz (1998), Nonlinear refraction traveltime tomography, *Geophysics*, *63*(5),
969 1726-1737.

970

971 Tables

972 Table 1: Travel-time picking uncertainties assigned to the WE-1 and ISE-1 datasets, and the
973 average picking uncertainties.

Dataset	Pick uncertainty (relative to instrument offset)	Average pick uncertainty
WE-1 (16 s)	40 ms + 1.5 ms/km	± 60.0 ms
WE-1 (64 s)	30 ms + 1.0 ms/km	± 54.9 ms
ISE-1	30 ms + 0.5 ms/km	± 44.6 ms

974

975 Table 2: Misfit statistics of the inverse tomography modeling.

	Travel time picks	RMS travel time misfit	Chi-square (χ^2)
Overall	10,717	53 ms	0.97
Refracted arrivals (Pg, Pb and Pn)	9,530	55 ms	1.01
S-reflection arrivals (PmP east)	1,187	31 ms	0.65
PmP arrivals (PmP west)	100	65 ms	-

976

977 Figure captions

978 Figure 1: A) Bathymetric map of the North Atlantic Ocean, showing the conjugate
979 Newfoundland and Iberia rifted margins. Inset shows the location of SCREECH seismic lines,
980 indicated by black lines [*Funck et al.*, 2003; *Shillington et al.*, 2006; *Van Avendonk et al.*,
981 2006]. Red circles indicate the location of ODP boreholes. B) Magnetic anomaly map [*Maus*
982 *et al.*, 2009] over the Iberia rift margin. Previous seismic experiments are illustrated by grey
983 lines, GP [*Reston et al.*, 1996; *Whitmarsh et al.*, 1996], ISE [*Sawyer et al.*, 1997], IAM [*Pickup*
984 *et al.*, 1996; *Dean et al.*, 2000] and CAM144 [*Chian et al.*, 1999]. Picks of isochron C34 are
985 shown as white circles [*Klitgord and Schouten*, 1986]. White dashed line represents the
986 interpreted location of magnetic anomaly M0 [*Srivastava et al.*, 2000], yellow dashed line
987 represents the interpreted location of magnetic anomaly M3 [*Whitmarsh and Miles*, 1995]. Red

dashed lines represent the location of the interpreted J anomaly [*Beslier et al.*, 1993]. C) Map of the Galicia-3D seismic experiment. ODP Leg 103 sites are indicated by red circles [*Boillot et al.*, 1987]. ISE-1 shooting profile is indicated by a green line; ISE-1 OBH are illustrated by blue triangles [*Zelt et al.*, 2003]. WE-1 shooting profile is illustrated by a red line; large black circles indicate the location of WE-1 OBS/H.

Figure 2: Data comparison between Galicia-3D OBS (43) and ISE-1 OBH (104), highlighting the additional noise introduced by a sub-optimal shooting in interval (~16 s) and smaller source array. These instruments are located within 1.3 km of one another and should exhibit seismic arrivals from common subsurface structure.

Figure 3: Observed and modeled data for instruments 74, 76, 78, 104 and 109. Top panels: Receiver gathers limited to offsets exhibiting identifiable first arrivals. Receiver gathers are filtered using a minimum phase Ormsby band-pass filter (2-4-8-16 Hz). Middle panels: Receiver gathers with observed and calculated travel times illustrated. Green bars indicate seismic arrival picks and their associated uncertainty, blue squares indicate the calculated travel times through the final velocity model. Bottom: Calculated ray paths through final TOMO2D velocity model. Thick black lines are the resolved S-reflector from TOMO2D modeling. White inverted triangles illustrate the location of ocean bottom instruments. Plots of the velocity model have a vertical exaggeration of 4.5.

Figure 4: Sediment velocity model. From top to bottom: ray paths of inter-sedimentary reflections, ray paths of refractions through the lower sedimentary layer, ray paths of basement reflections, fit of calculated travel times (colored points) with observed travel times (black points).

Figure 5: Top: Input velocity model to the TOMO2D joint inversion process. Solid black line represents the arbitrary surface representing the S-reflector. Bottom: Final TOMO2D velocity

model after 10 inversion iterations. Solid black line represents the modified S-reflector after the inversion process. White inverted triangles illustrate the location of ocean bottom instruments used in this inversion process, a select number of instruments are labelled. Black vertical lines of varying thickness and dashes indicate the location of 1D velocity profiles illustrated in Figure 12. Plots have a vertical exaggeration of 4.5.

Figure 6: Travel time misfit between the observed seismic travel times and the calculated travel times through the input (top) and final (bottom) compressional velocity models. Travel time misfit is plotted against absolute offset from the recording instrument as black points.

Figure 7: Derivative weight sum of seismic rays traced through the TOMO2D velocity model. Higher DWS values indicate areas where a higher density of rays have sampled model cells. Thick black line is the S-reflector. Vertical dashed line indicates the axis of the Peridotite Ridge. Black inverted triangles illustrate the location of ocean bottom instruments. Select instrument numbers are indicated. Plots have a vertical exaggeration of 4.5.

Figure 8: Monte Carlo uncertainty test results. Top: Average velocity model from the 100 model realizations. Thick black line illustrates the average S-reflector surface. Bottom: Velocity uncertainty of the average velocity model. Uncertainty is taken as one standard deviation of the 100 model realizations from the average velocity model. Gray envelope represents the range of all resolved S-reflection surfaces. Black inverted triangles illustrate the location of ocean bottom instruments. Plots have a vertical exaggeration of 4.5.

Figure 9: Checkerboard resolution test results. Top: input velocity anomalies for the 25 x 5 km checkerboard in order to demonstrate the boundaries between cells. Recovered velocity anomalies from the checkerboard tests are below. Second from top to bottom the anomaly dimensions are: 25 x 5 km, 10 km x 5 km, 10 km x 2.5 km and 5 km x 2.5 km, horizontally

and vertically, respectively. Vertical dashed line indicates the axis of the Peridotite Ridge. Plots have a vertical exaggeration of 4.5.

Figure 10: Modeled depth of the Moho from limited PmP arrivals on instruments 73, 74, 75 and 76, west of the Peridotite Ridge. Above: Receiver gathers from instrument 74; green bars indicate PmP travel time picks and their associated uncertainties; blue squares indicate the modeled travel times through the velocity model; red line illustrates wide-angle basement reflection. Below: Final compressional velocity model, limited to 30 – 70 km profile distance, illustrating the resolved Moho boundary. The location of M0 (vertical white dashed line) is as interpreted by *Srivastava et al.* [2000].

Figure 11: Results of the gravity modeling. Top: Small black dots illustrate the misfit between observed and calculated free-air gravity anomalies, black line shows the linear trend fitted to this misfit, which represents the regional gravity trend. Middle: Black line shows the observed ship-borne free-air gravity anomaly, small red circles show the calculated free-air gravity anomaly, large blue circles show the regionally corrected free-air gravity anomaly calculations. Bottom: Extended density model. Region A is the density model converted from the final TOMO2D velocity model. Region B is the density model converted from the compressional velocity model of *Zelt et al.* [2003]. Region C is an extrapolation of the 1D density profile from 30 km profile distance. Region D is an extrapolation of mantle densities to 25 km depth in order to match the depth of region. Plot has a vertical exaggeration of 9.

Figure 12: 1D velocity profiles through the final TOMO2D velocity model (Figure 5). Light blue shading indicates the depths at which the Moho, below oceanic crust, is identified. Left: 1D velocity profiles compared to the velocity envelope for Atlantic oceanic crust aged 59 - 170 Ma [White et al., 1992]. Center: 1D velocity profiles compared to the velocity envelope for velocity models within the COT from previous studies, as compiled by *Minshull*

[2009]. Right: 1D velocity profiles compared with velocity profiles through thin oceanic crust on the SCREECH-1 compressional velocity model of *Funck et al.* [2003] (green dashed lines) and the GP101 model of *Whitmarsh et al.* [1996] (red dashed line).

Figure 13: Top: Kirchhoff time-migrated multichannel seismic image of WE-1 from *Dean et al.* [2015]. Normal faults F3 – F7, identified on the coincident ISE-1 profile by *Borgmeyer* [2010], are indicated east of the Peridotite Ridge with arrows. Ridge structures identified west of the Peridotite Ridge by *Dean et al.* [2015], are indicated by arrows. M0 magnetic anomaly is indicated by a dashed black line [*Srivastava et al.*, 2000]. Bottom: The same image overlain by the time-converted compressional velocity model. White inverted triangles illustrate the location of ocean bottom instruments. Thick dashed black line illustrates the time converted S-reflector; thick black line illustrates areas where the Moho is sampled.

Figure 14: Comparison of existing velocity models east of the Peridotite Ridge, and their correlation with reflection seismic interpretations. A) Velocity model from *Zelt et al.* [2003] along ISE-1. B) Slice through 3D model of *Bayrakci et al.* [2016] using Galicia-3D data. C) Final TOMO2D velocity model along WE-1. Horizon and fault surfaces are from interpretations of depth migrated images along ISE-1 in *Borgmeyer* [2010], and GP12 in *Reston et al.* [1996]. Thick solid black line is the S-reflector resolved by the reflected rays (thin black lines) from the TOMO2D inversion process. Inverted triangles are instruments used to resolve the S-reflector. Plots have a vertical exaggeration of 3.

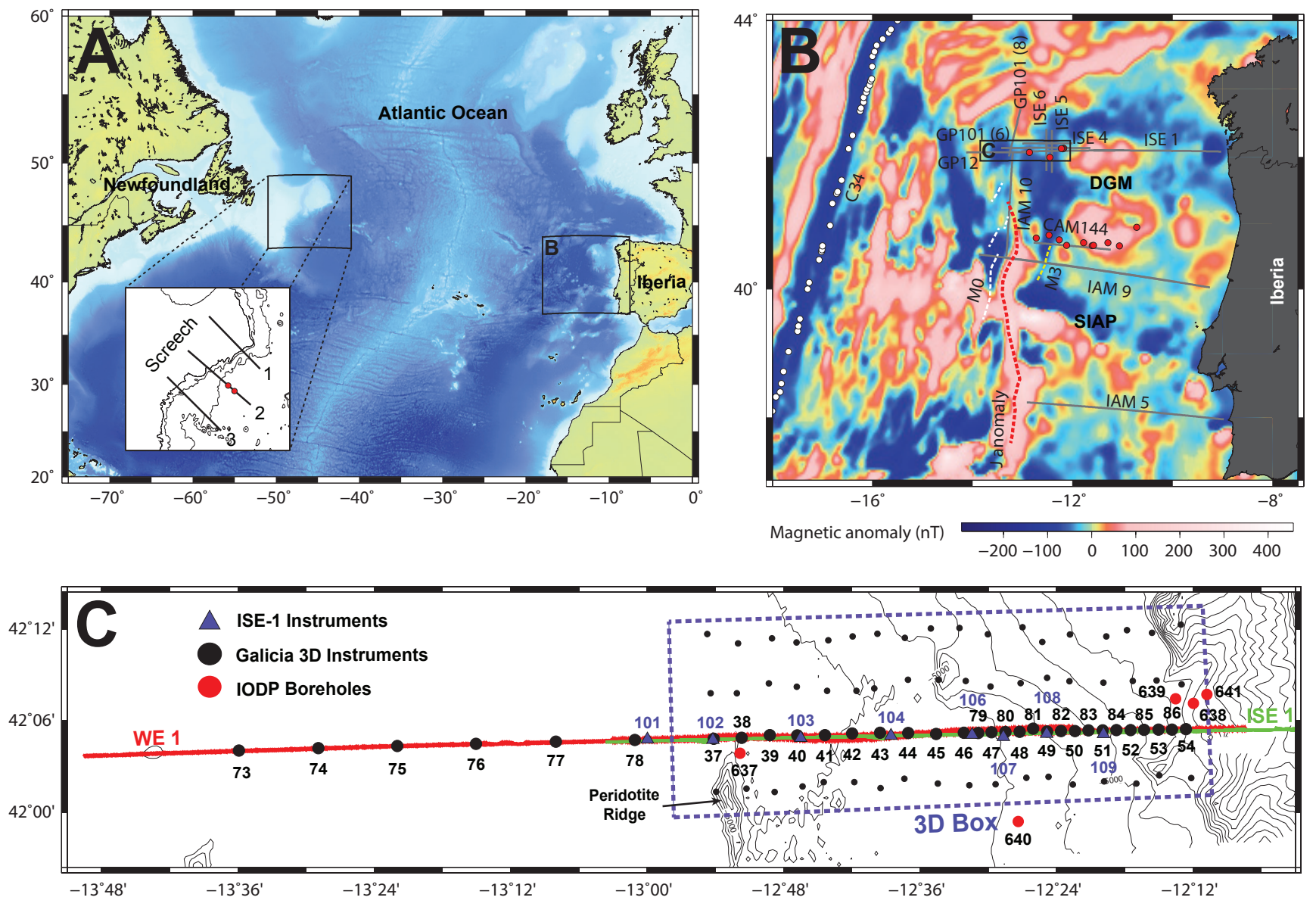
A
Atlantic Ocean
Newfoundland
Iberia
B
Screech
1
2
3
60°
50°
40°
30°
20°
−70°
−60°
−50°
−40°
−30°
−20°
−10°
0°
B
GP101 (8)
ISE 6
ISE 5
GP101 (6)
GP12
C
ISE 4
ISE 1
DGM
C34
IAM 10
CAM144
M0
M3
IAM 9
SIAP
Iberia
Jahomaly
IAM 5
44°
40°
−16°
−12°
−8°
Magnetic anomaly (nT)
−200 −100 0 100 200 300 400
C
ISE-1 Instruments
Galicia 3D Instruments
IODP Boreholes
WE 1
73
74
75
76
77
78
101
102
38
103
104
106
108
639
641
79
80
81
82
83
84
85
86
638
ISE 1
37
637
39
40
41
42
43
44
45
46
47
48
49
50
51
52
53
54
107
109
Peridotite
Ridge
3D Box
640
42°12'
42°06'
42°00'
−13°48'
−13°36'
−13°24'
−13°12'
−13°00'
−12°48'
−12°36'
−12°24'
−12°12'

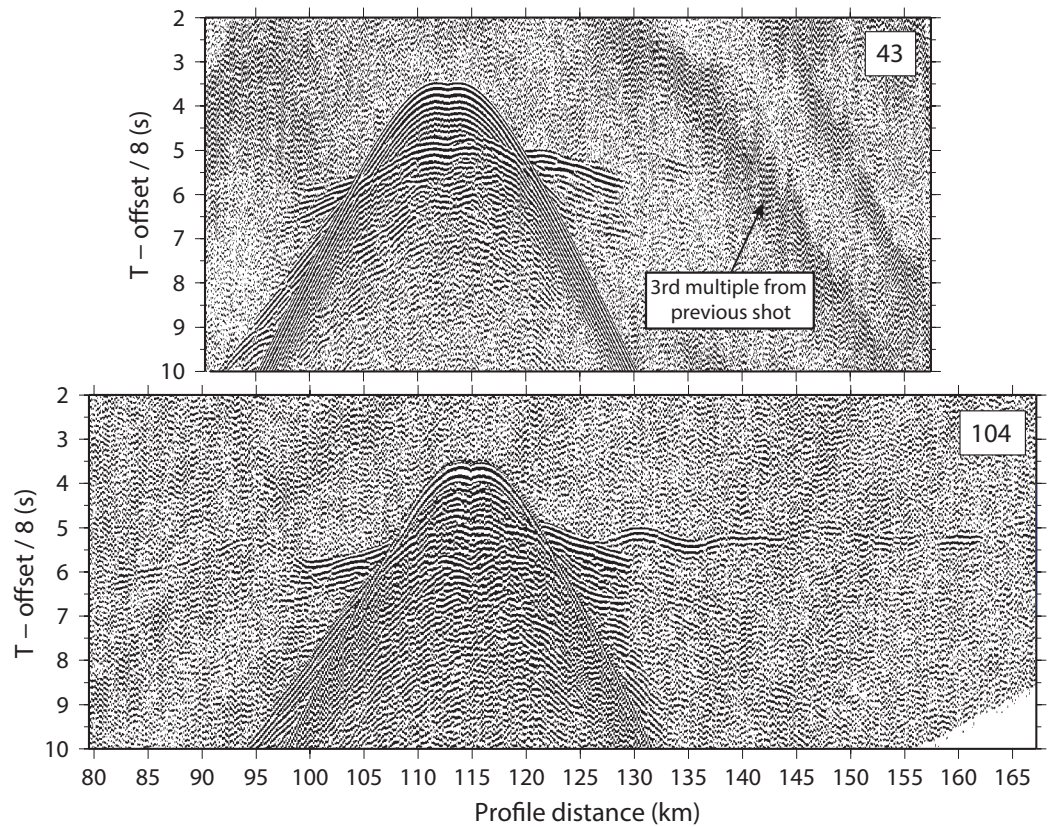
43
3rd multiple from previous shot
T – offset / 8 (s)
104
T – offset / 8 (s)
Profile distance (km)

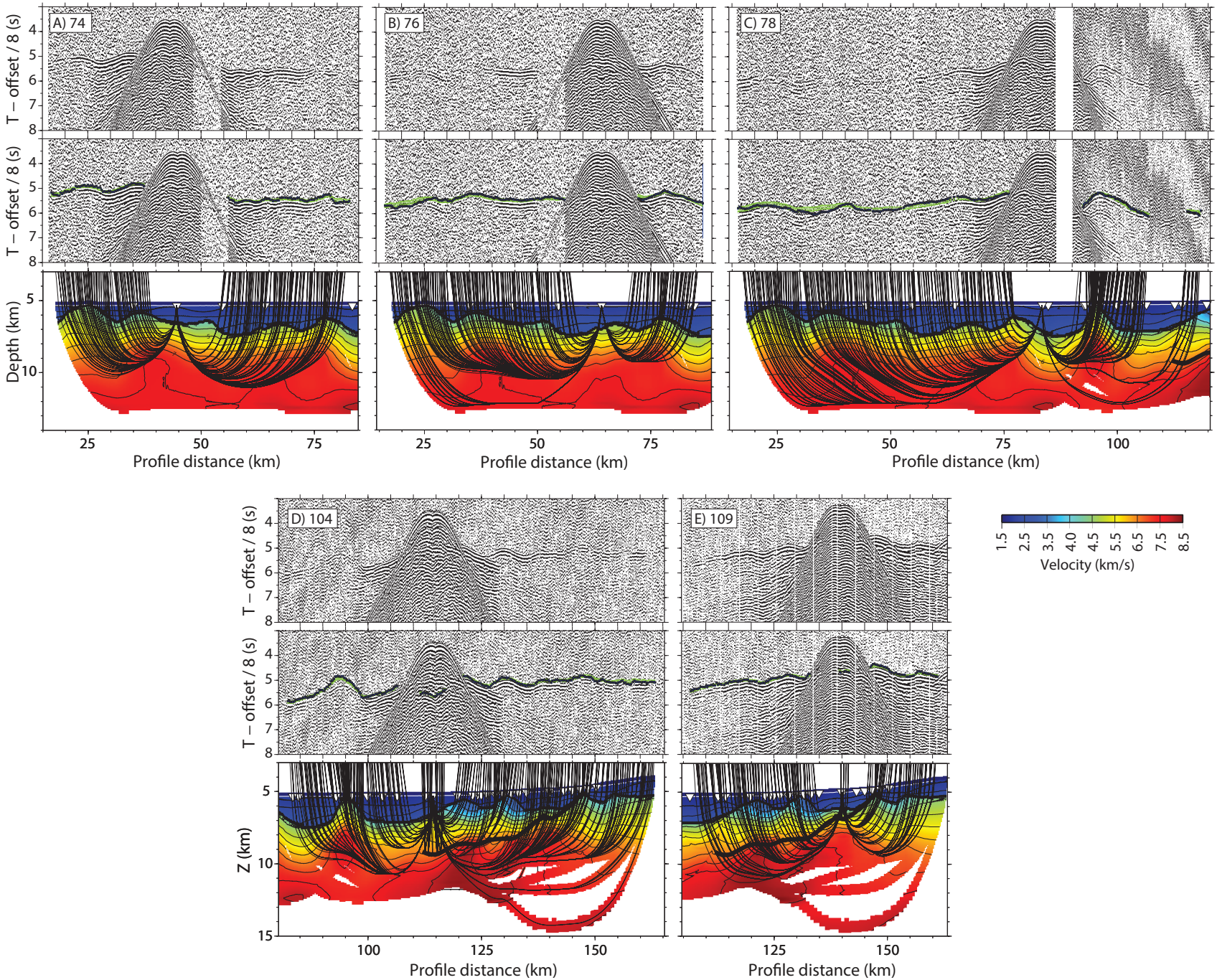
A) 74
B) 76
C) 78
D) 104
E) 109
T – offset / 8 (s)
Depth (km)
Z (km)
Profile distance (km)
Velocity (km/s)
1.5
2.5
3.5
4.0
4.5
5.5
6.5
7.5
8.5

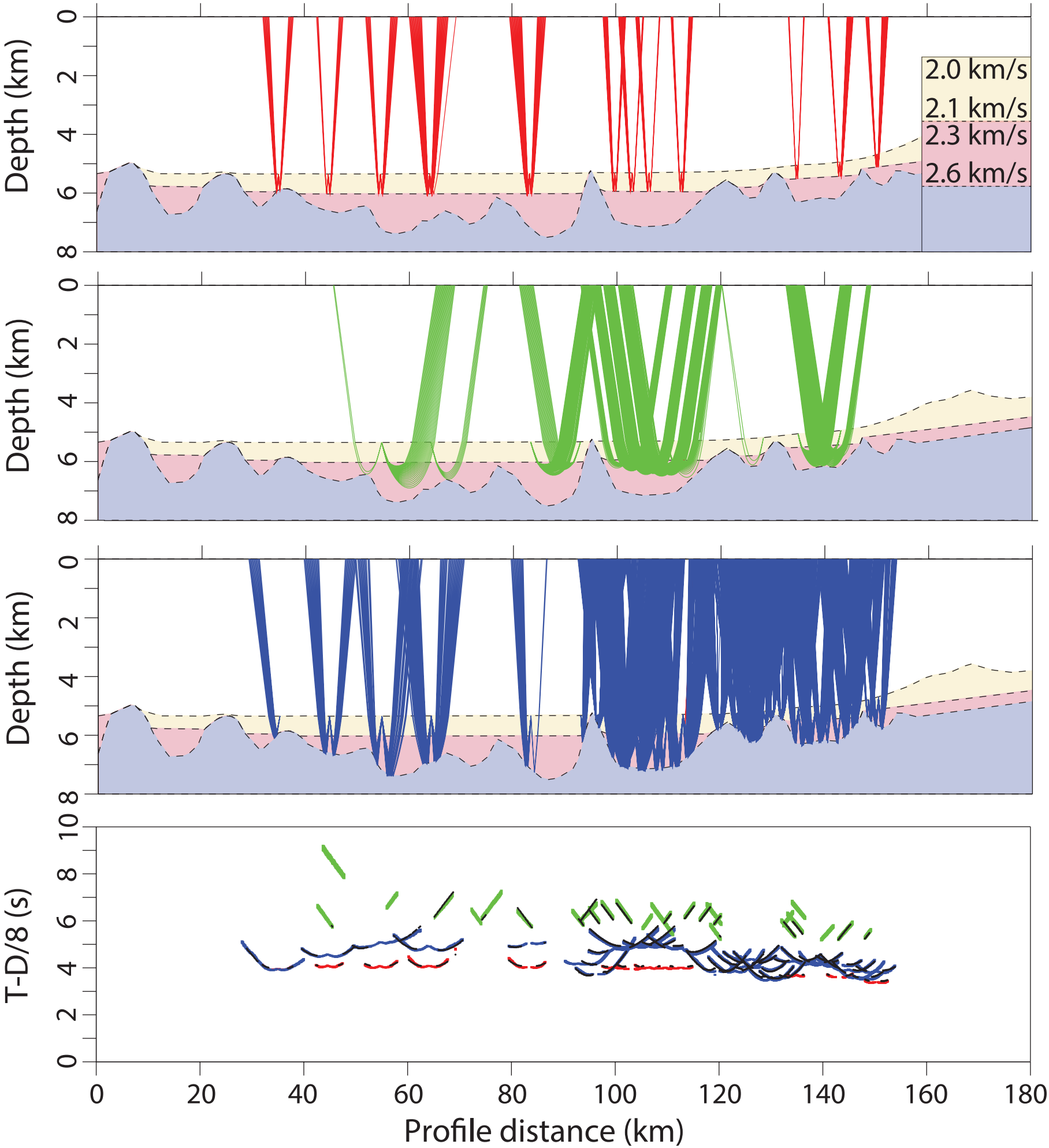
Depth (km)
0
2
4
6
8
2.0 km/s
2.1 km/s
2.3 km/s
2.6 km/s
Depth (km)
0
2
4
6
8
Depth (km)
0
2
4
6
8
T-D/8 (s)
0
2
4
6
8
10
0
20
40
60
80
100
120
140
160
180
Profile distance (km)

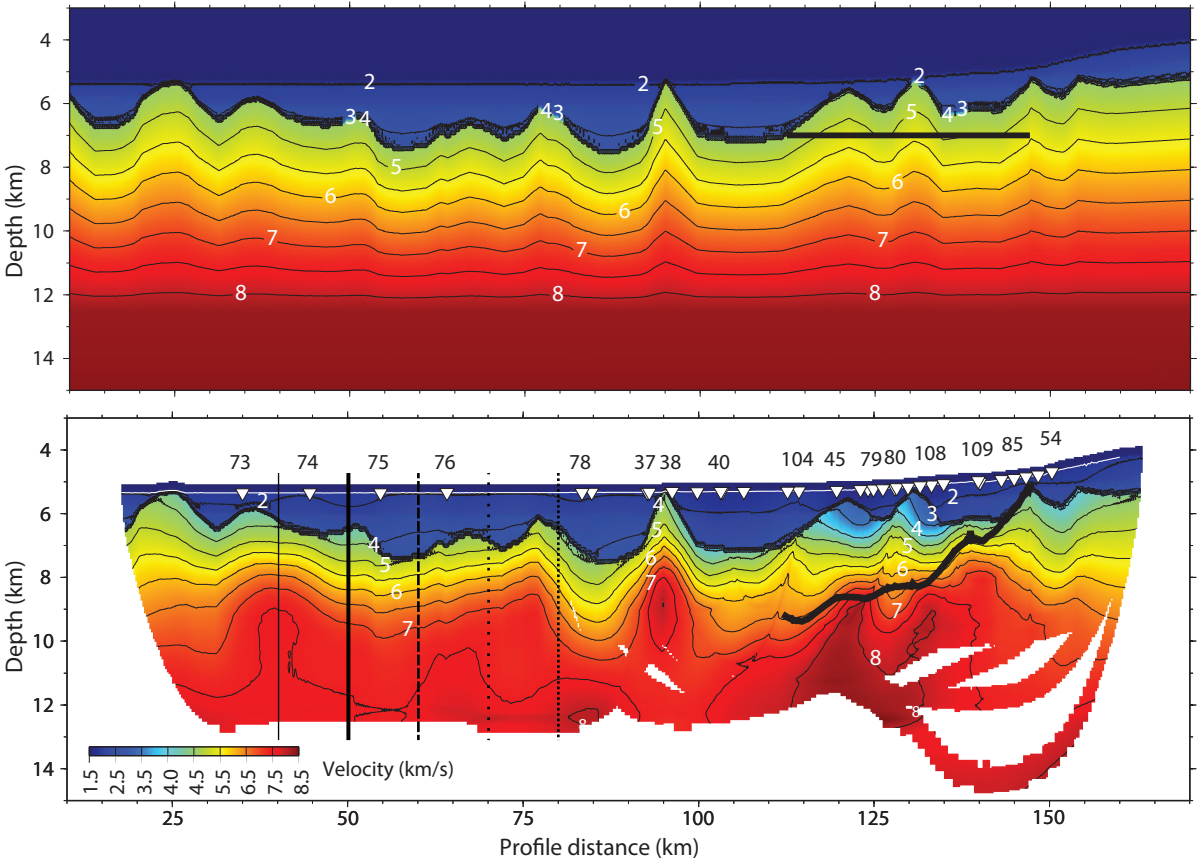
Depth (km)
4
6
8
10
12
14
2
3
4
5
6
7
8
73
74
75
76
78
37
38
40
104
45
79
80
108
109
85
54
1.5
2.5
3.5
4.0
4.5
5.5
6.5
7.5
8.5
Velocity (km/s)
25
50
75
100
125
150
Profile distance (km)

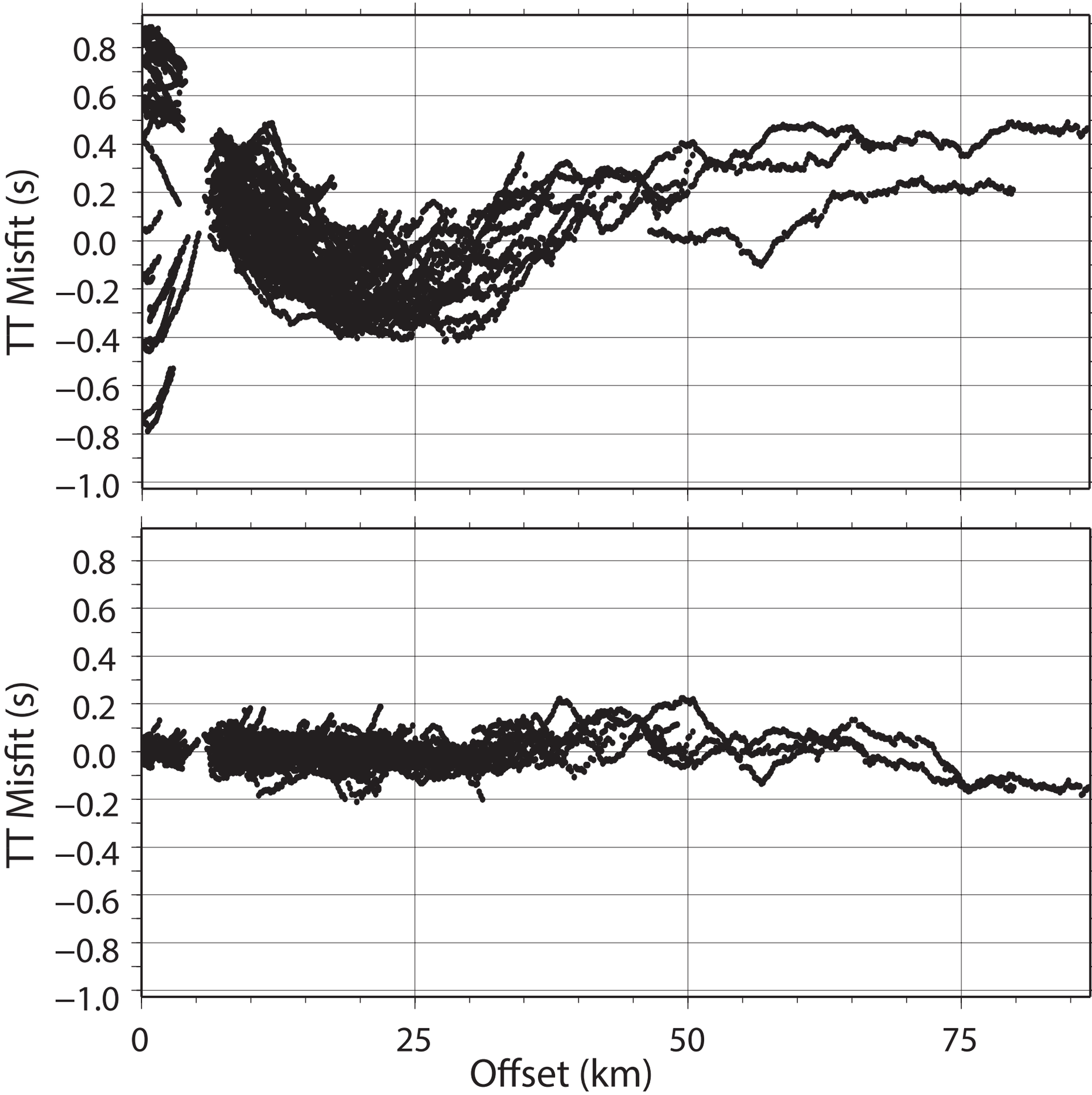
TT Misfit (s)
0.8
0.6
0.4
0.2
0.0
−0.2
−0.4
−0.6
−0.8
−1.0
TT Misfit (s)
0.8
0.6
0.4
0.2
0.0
−0.2
−0.4
−0.6
−0.8
−1.0
0
25
50
75
Offset (km)

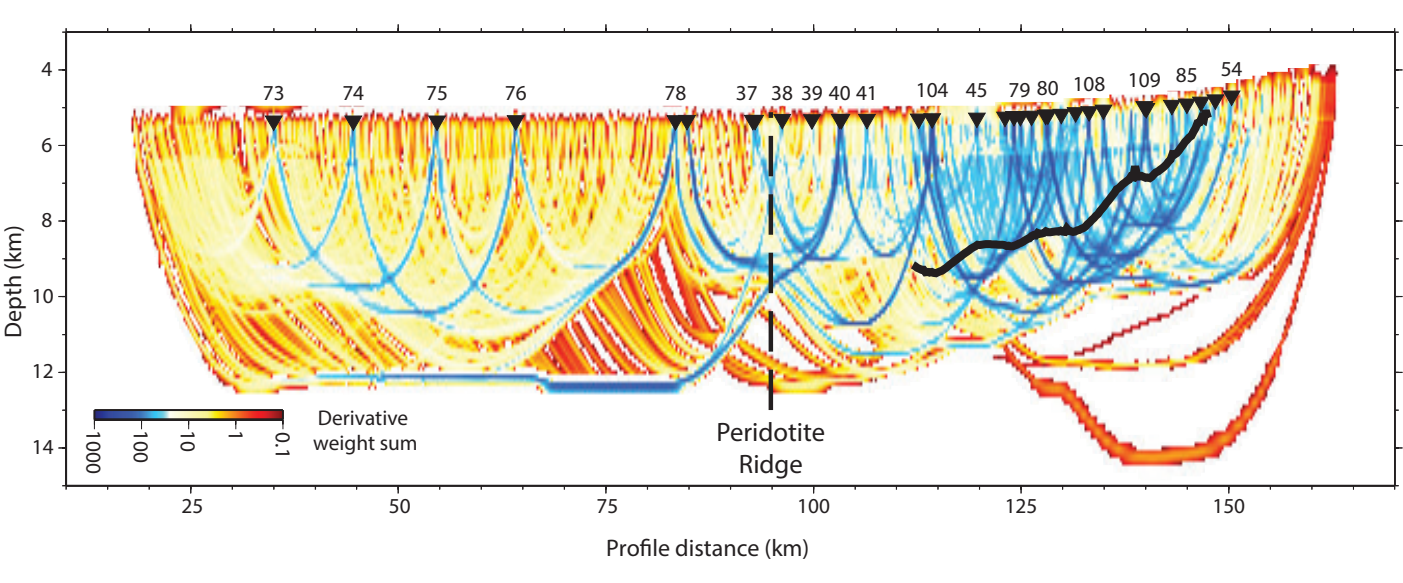
Depth (km)
4
6
8
10
12
14
73
74
75
76
78
37
38
39
40
41
104
45
79
80
108
109
85
54
Derivative
weight sum
1000
100
10
1
0.1
Peridotite
Ridge
25
50
75
100
125
150
Profile distance (km)

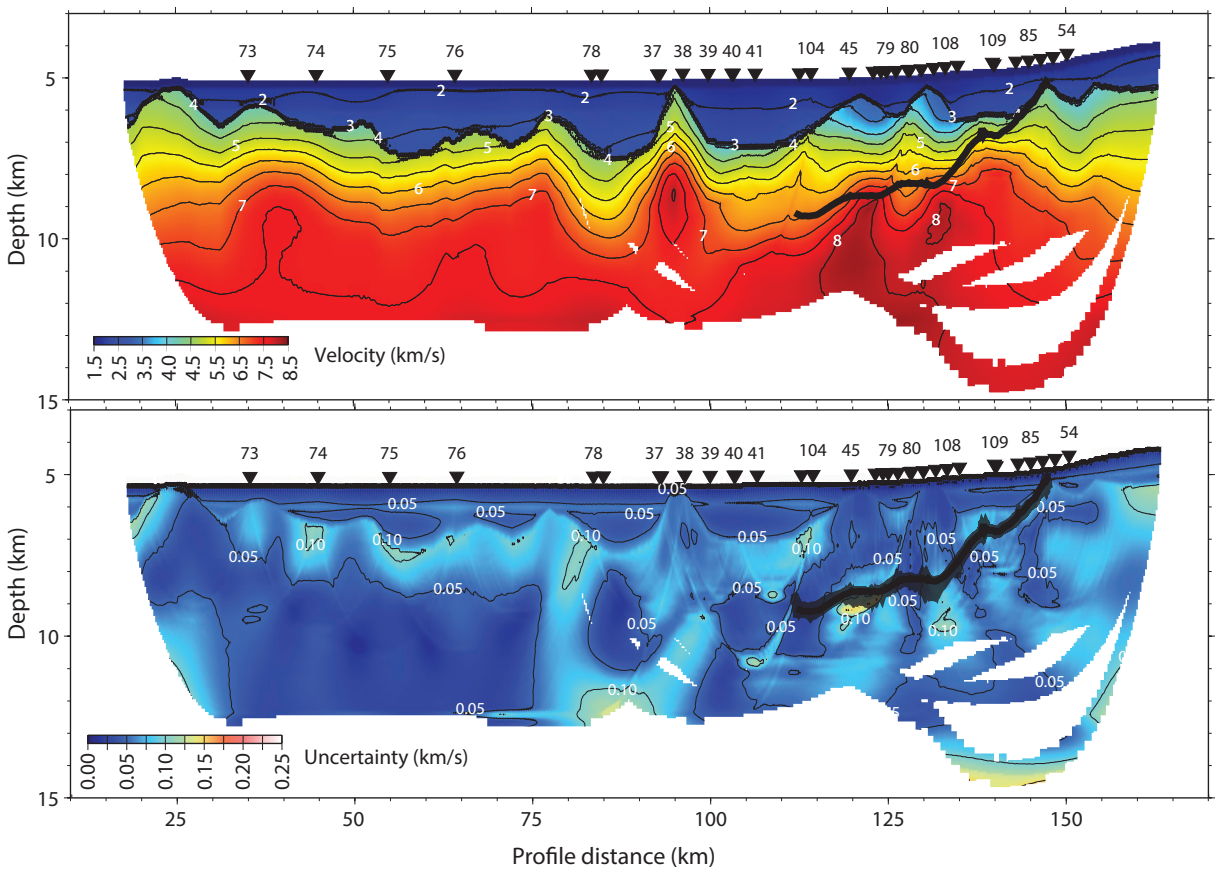
73 74 75 76 78 37 38 39 40 41 104 45 79 80 108 109 85 54
Depth (km)
5
10
15
1.5 2.5 3.5 4.0 4.5 5.5 6.5 7.5 8.5
Velocity (km/s)
0.00 0.05 0.10 0.15 0.20 0.25
Uncertainty (km/s)
25 50 75 100 125 150
Profile distance (km)

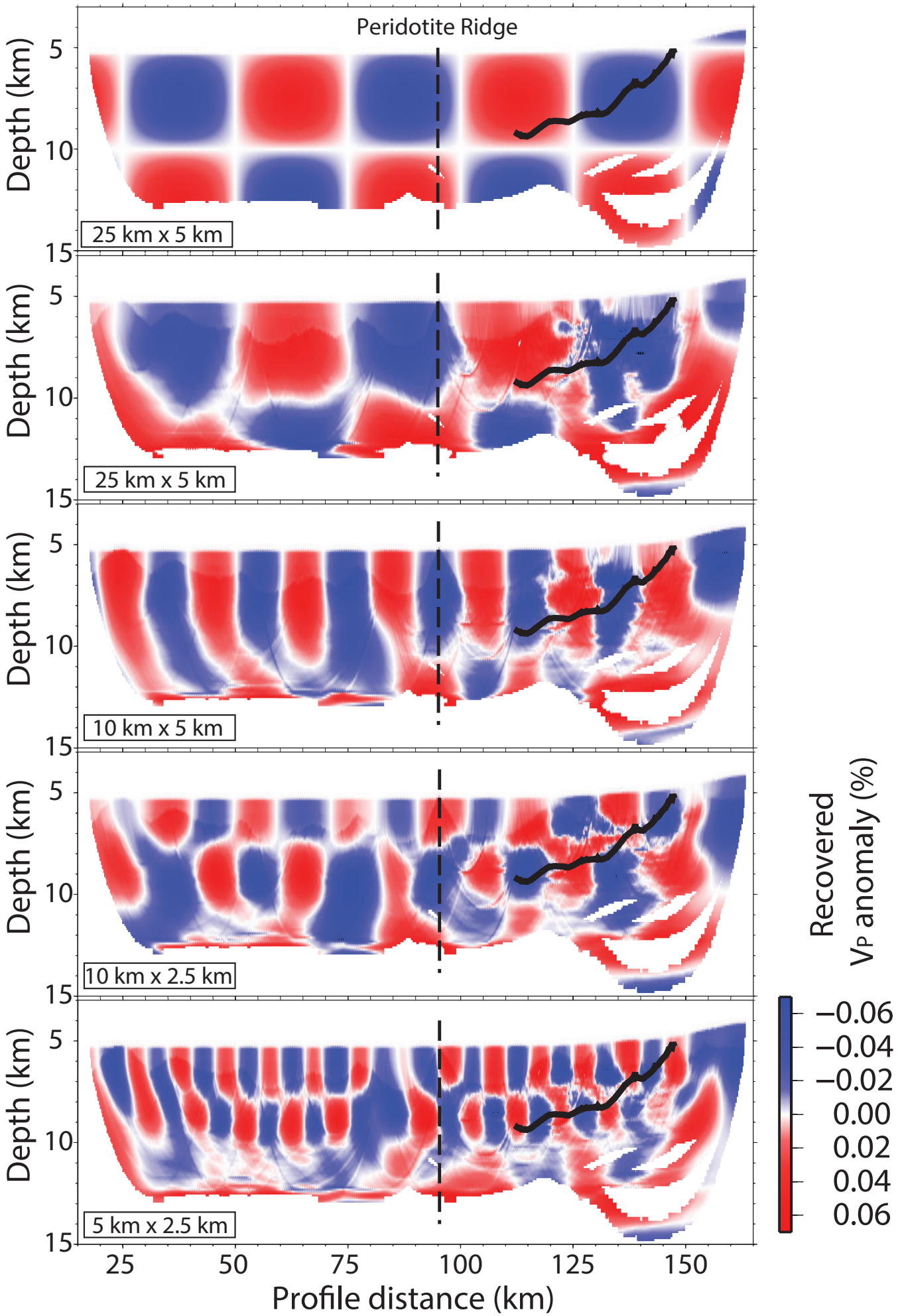
Peridotite Ridge
Depth (km)
5
10
15
25 km x 5 km
25 km x 5 km
10 km x 5 km
10 km x 2.5 km
5 km x 2.5 km
25
50
75
100
125
150
Profile distance (km)
Recovered
VP anomaly (%)
−0.06
−0.04
−0.02
0.00
0.02
0.04
0.06

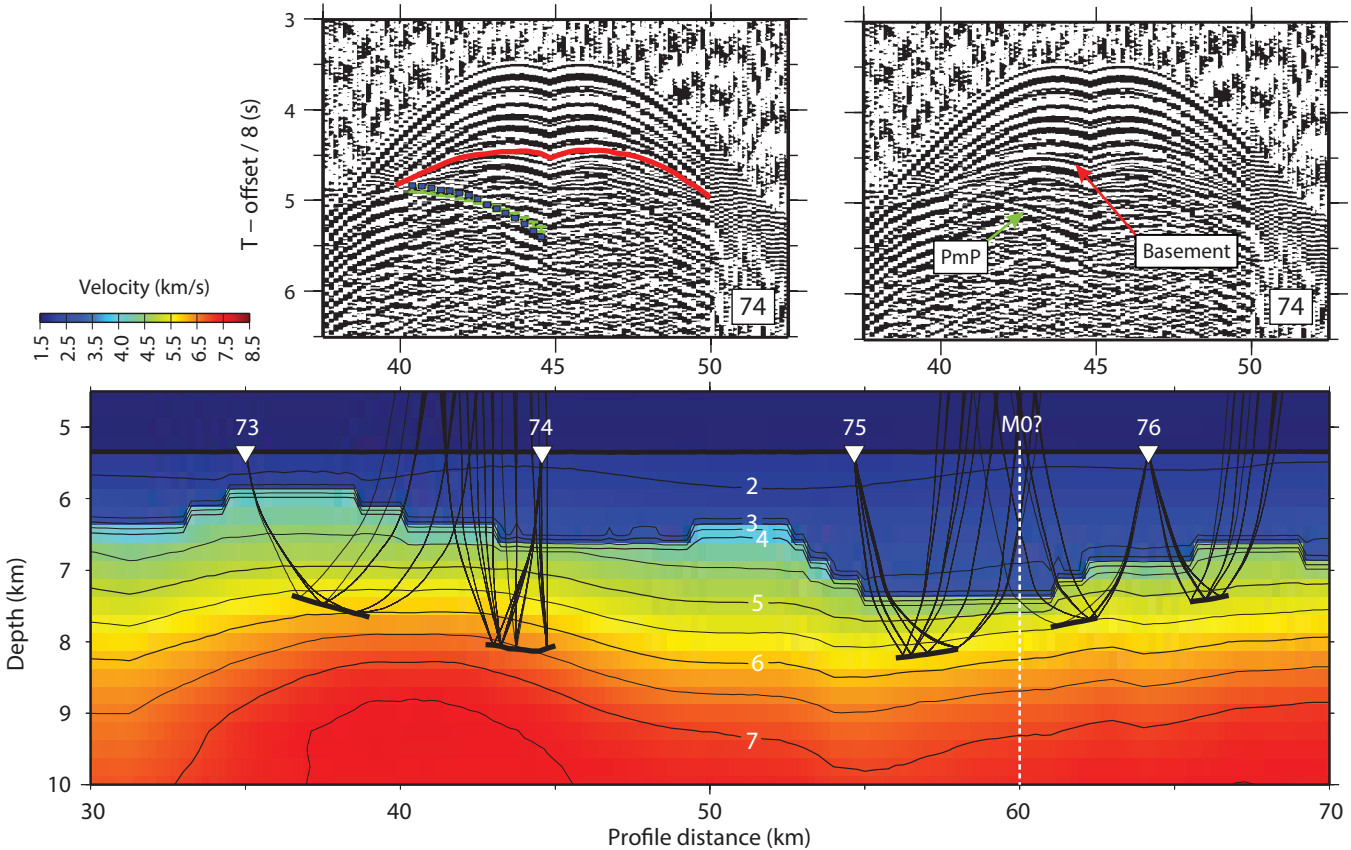
T – offset / 8 (s)
3
4
5
6
40
45
50
74
PmP
Basement
Velocity (km/s)
1.5
2.5
3.5
4.0
4.5
5.5
6.5
7.5
8.5
73
74
75
M0?
76
2
3
4
5
6
7
Depth (km)
5
6
7
8
9
10
30
40
50
60
70
Profile distance (km)

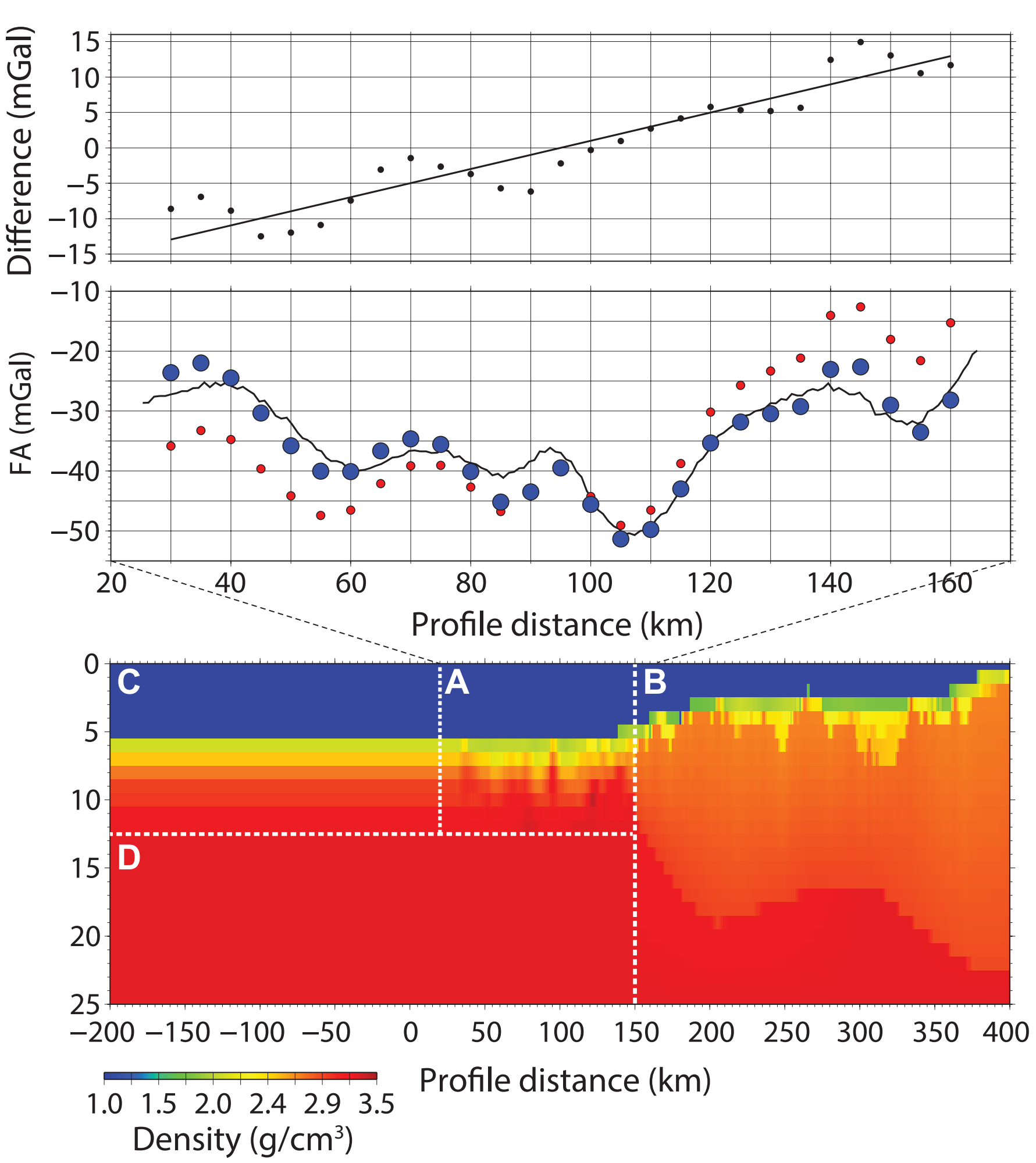
Difference (mGal)
15
10
5
0
−5
−10
−15
FA (mGal)
−10
−20
−30
−40
−50
20
40
60
80
100
120
140
160
Profile distance (km)
C
A
B
D
0
5
10
15
20
25
−200
−150
−100
−50
0
50
100
150
200
250
300
350
400
Profile distance (km)
1.0
1.5
2.0
2.4
2.9
3.5
Density (g/cm³)

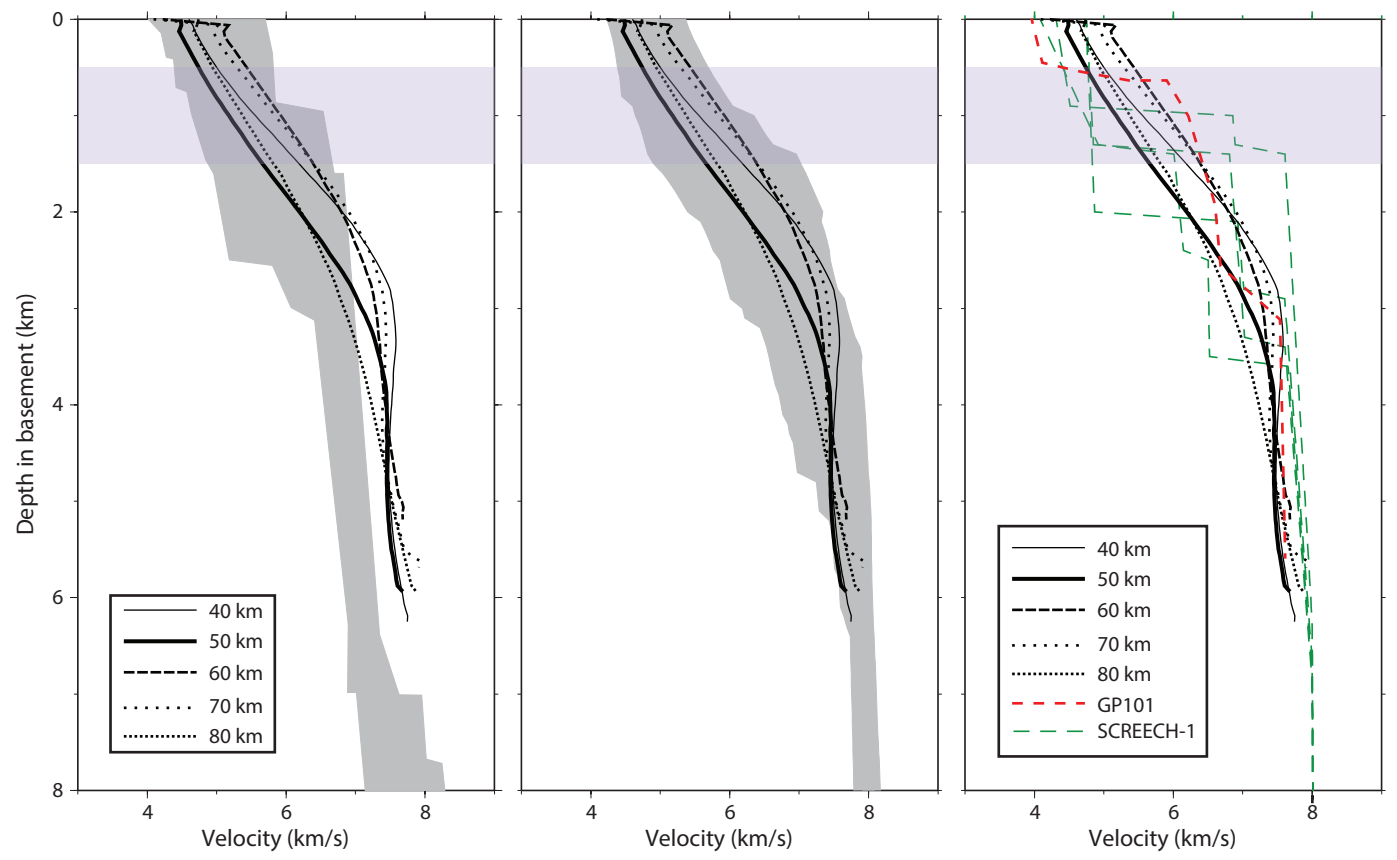
Depth in basement (km)
0
2
4
6
8
4
6
8
Velocity (km/s)
40 km
50 km
60 km
70 km
80 km
GP101
SCREECH-1

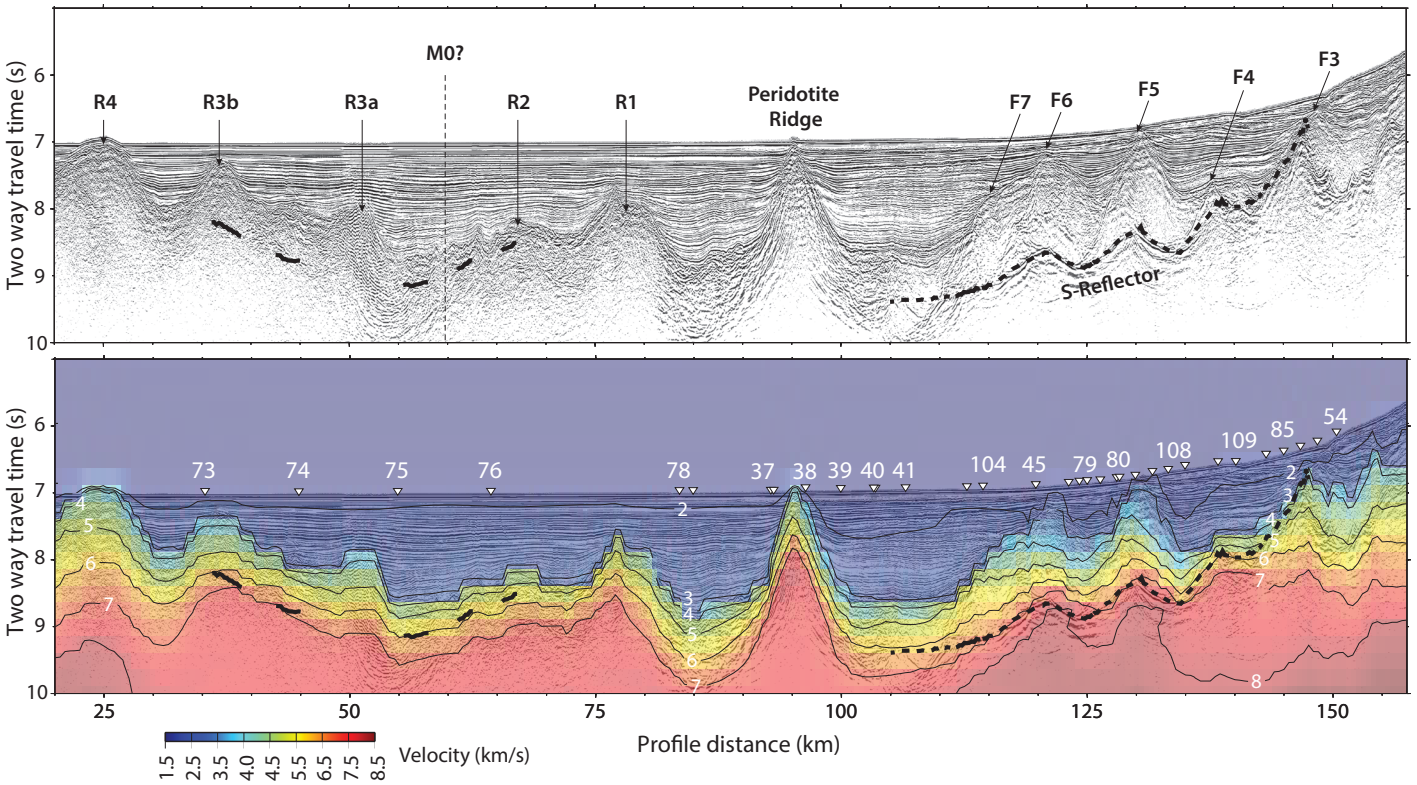
R4
R3b
R3a
M0?
R2
R1
Peridotite Ridge
F7
F6
F5
F4
F3
S-Reflector
Two way travel time (s)
6
7
8
9
10
73
74
75
76
78
37
38
39
40
41
104
45
79
80
108
109
85
54
25
50
75
100
125
150
Profile distance (km)
Velocity (km/s)
1.5
2.5
3.5
4.0
4.5
5.5
6.5
7.5
8.5

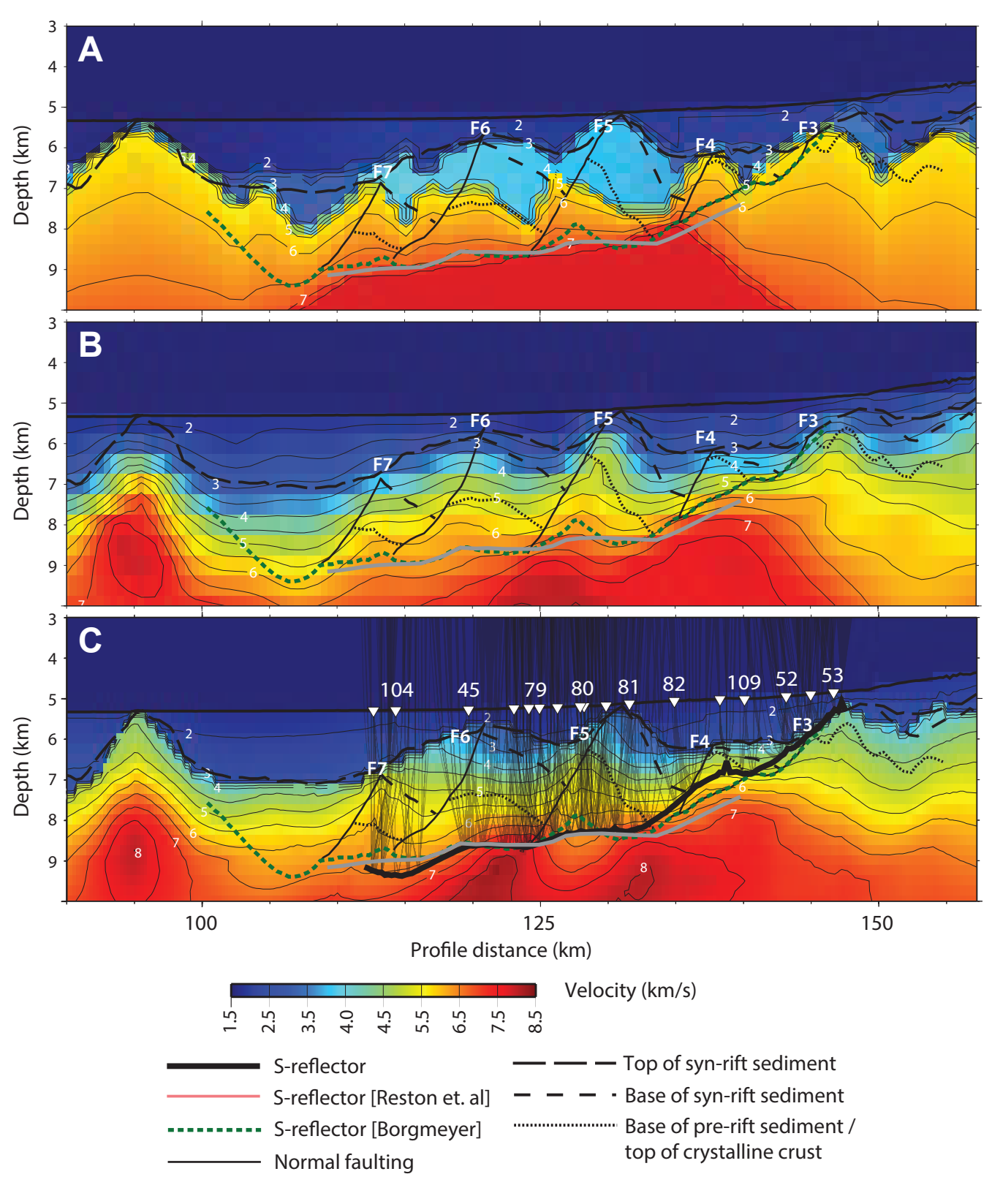
A
B
C
F3
F4
F5
F6
F7
104
45
79
80
81
82
109
52
53
Depth (km)
Profile distance (km)
100
125
150
Velocity (km/s)
1.5
2.5
3.5
4.0
4.5
5.5
6.5
7.5
8.5
S-reflector
S-reflector [Reston et. al]
S-reflector [Borgmeyer]
Normal faulting
Top of syn-rift sediment
Base of syn-rift sediment
Base of pre-rift sediment / top of crystalline crust